Thesis for the degree of Doctor of Philosophy

Switchable and tunable bulk acoustic wave resonators based on $Ba_xSr_{1-x}TiO_3$ thin films

John Berge

CHALMERS

Terahertz and Millimetre Wave Laboratory
Department of Microtechnology and Nanoscience (MC2)
Chalmers University of Technology
Göteborg, Sweden, 2012

Switchable and tunable bulk acoustic wave resonators
based on $Ba_xSr_{1-x}TiO_3$ thin films

John Berge
ISBN 978-91-7385-643-0

Doktorsavhandlingar vid Chalmers tekniska högskola
Ny serie #3324
ISSN 0346-718X

Technical Report MC2-215
ISSN 1652-0769

Chalmers University of Technology
Department of Microtechnology and Nanoscience (MC2)
Terahertz and Millimetre Wave Laboratory
SE–412 96 Göteborg, Sweden
Phone: +46 (0) 31 772 1000

Cover: Smith chart showing response of $Ba_{0.25}Sr_{0.75}TiO_3$ TFBAR at different dc bias voltages.

Printed by Chalmers Reproservice
Göteborg, Sweden, 2012

Abstract

The main focus of this thesis is the study of a novel microwave component, the tunable thin film bulk acoustic wave resonator (TFBAR), based on ferroelectric $Ba_xSr_{1-x}TiO_3$ thin films.

Conventional fixed frequency TFBARs, widely used for filtering applications in wireless communication systems, are based on ordinary piezoelectrics. The tunable TFBAR on the other hand utilizes the dc field induced piezoelectric effect in the ferroelectric film. This allows dc field tuning of the resonance frequency as well as switching between resonator and capacitor response.

A brief introduction to the $Ba_xSr_{1-x}TiO_3$ material system is given, followed by results from thin films grown by pulsed laser deposition. Effects of substrate temperature and ambient gas pressure during growth are discussed.

Resonator design and fabrication issues are covered, including studies of electrode configurations and acoustic mirror structures. Measurement results are presented in wide dc bias and temperature ranges. The achieved room temperature tuning range for a 5.7 GHz $Ba_{0.25}Sr_{0.75}TiO_3$ TFBAR is 3.8% and the effective electromechanical coupling coefficient at maximum bias is 7.1%, with a Q-factor of 130.

A switchable bandpass filter is considered as a possible application of $Ba_xSr_{1-x}TiO_3$ TFBARs. Simulated filter characteristics and preliminary results from fabricated filters are presented.

Keywords: Ferroelectric thin films, tunable microwave devices, bulk acoustic wave devices, piezoelectric resonators, field induced piezoelectric effect.

List of publications

Appended papers

[A] J. Berge, A. Vorobiev, and S. Gevorgian, "Impact of thin film roughness on the performance of tunable bulk acoustic wave resonators," *Manuscript.*

[B] J. Berge and S. Gevorgian, "Tunable bulk acoustic wave resonators based on $Ba_{0.25}Sr_{0.75}TiO_3$ thin films and a HfO_2/SiO_2 Bragg reflector," *IEEE Trans. Ultrason. Ferroelectr. Freq. Control*, vol. 58, no. 12, pp. 2768–2771, 2011.

[C] J. Berge, M. Norling, A. Vorobiev, and S. Gevorgian, "The effect of Bragg reflectors on the electromechanical performance of parallel-plate ferroelectric capacitors," *IOP Conf. Ser.: Mater. Sci. Eng.*, vol. 8, no. 1, pp. 012011–1–4, 2010.

[D] J. Berge, M. Norling, A. Vorobiev, and S. Gevorgian, "Field and temperature dependent parameters of the dc field induced resonances in $Ba_xSr_{1-x}TiO_3$-based tunable thin film bulk acoustic resonators," *J. Appl. Phys.*, vol. 103, no. 6, pp. 064508–1–8, 2008.

[E] J. Berge, A. Vorobiev, W. Steichen, and S. Gevorgian, "Tunable solidly mounted thin film bulk acoustic resonators based on $Ba_xSr_{1-x}TiO_3$ films," *IEEE Microw. Wireless Compon. Lett.*, vol. 17, no. 9, pp. 655–657, 2007.

[F] J. Berge, A. Vorobiev, and S. Gevorgian, "The effect of growth temperature on the nanostructure and dielectric response of $BaTiO_3$ ferroelectric films," *Thin Solid Films*, vol. 515, no. 16, pp. 6302–6308, 2007.

Other publications

[a] A. Vorobiev, J. Berge, S. Gevorgian, M. Löffler, and E. Olsson, "Effect of interface roughness on acoustic loss in tunable thin film bulk acoustic wave resonators," *J. Appl. Phys.*, vol. 110, no. 2, pp. 024116–1–4, 2011.

[b] A. Vorobiev, J. Berge, M. Norling, and S. Gevorgian, "Silicon substrate integration of BST based tunable TFBARs using all-dielectric SiO_2/AlN Bragg reflectors," in *Proc. IEEE SiRF*, 2010, pp. 41–44.

[c] M. Norling, J. Berge, and S. Gevorgian, "Parameter extraction for tunable TFBARs based on $Ba_xSr_{1-x}TiO_3$," in *IEEE MTT-S Int. Microw. Symp. Dig.*, 2009, pp. 101–104.

[d] S. Gevorgian, T. Lewin, A. Vorobiev, M. Norling, and J. Berge, "A voltage controlled switching device", *Patent* WO/2009/043370 (April 9 2009), Int. filing date Oct 1 2007.

[e] I. B. Vendik, P. A. Turalchuk, O. G. Vendik, and J. Berge, "Modeling tunable bulk acoustic resonators based on induced piezoelectric effect in $BaTiO_3$ and $Ba_{0.25}Sr_{0.75}TiO_3$ films," *J. Appl. Phys.*, vol. 103, no. 1, pp. 014107–1–6, 2008.

[f] P. Turalchuk, I. Vendik, O. Vendik, and J. Berge, "Electrically tunable bulk acoustic filters with induced piezoelectric effect in BSTO film," in *Proc. EuMC*, 2008, pp. 1695–1698.

[g] A. Vorobiev, J. Berge, and S. Gevorgian, "Thin film $Ba_{0.25}Sr_{0.75}TiO_3$ voltage tunable capacitors on fused silica substrates for applications in microwave microelectronics," *Thin Solid Films*, vol. 515, no. 16, pp. 6606–6610, 2007.

[h] P. Turalchuk, I. Vendik, O. Vendik, and J. Berge, "Modelling of tuneable acoustic resonators based on BSTO films with induced piezoelectric effect," in *Proc. EuMC*, 2007, pp. 282–285.

[i] A. Vorobiev, J. Berge, and S. Gevorgian, "Thin film $Ba_{0.25}Sr_{0.75}TiO_3$ varactors on Au bottom electrode for microwave applications," in *Proc. EuMC*, 2006, pp. 839–842.

[j] S. Gevorgian, A. Vorobiev, and J. Berge, "Electromechanical Modelling and Reduction of the Electroacoustic Losses in Parallel-Plate Ferroelectric Varactors," in *Proc. EuMC*, 2006, pp. 851–853.

Contents

Chapter 1

Introduction

This introductory chapter provides motivation for the work presented in this thesis, and a description of the thesis organization. Some background to the ferroelectric materials under consideration in this work is also given.

1.1 Motivation and thesis organization

This thesis is devoted to the study of ferroelectric $Ba_xSr_{1-x}TiO_3$ thin films and their use in tunable microwave devices. Reconfigurable technologies are expected to become increasingly important in order to meet present and future demands on improved and added functionalities of microwave devices. Modern mobile phones is an example where the combination of multi-standard cellular network capabilities, GPS receivers and WLAN connectivity, all operating in separate frequency bands, set strict requirements on the rf design.

The main focus of this work is a novel type of thin film bulk acoustic wave resonator (TFBAR) which due to the field dependent properties of the ferroelectric material presents switchable and tunable characteristics under dc bias. The principal functionality of this component has only recently been demonstrated, and it may potentially contribute to more cost effective, energy efficient, and compact microwave systems. This type of resonator may allow development of switchable filters which can simplify the signal path in multi-standard communication systems by eliminating separate switches. Truly tunable bandpass filters could bring even further advantages by replacing several fixed frequency filters and switches with one compact component. Another attractive application of tunable TFBARs is voltage controlled oscillators, where the potentially very high Q-factor of the tunable TFBAR could replace LC tanks based on lossy varactors.

The work presented mainly concerns development and studies of the resonator itself, including issues related to resonator design, fabrication

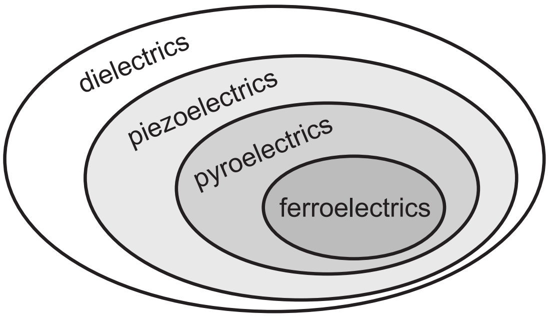

Fig. 1.1: The general class of dielectrics can be divided into subgroups of piezoelectric, pyroelectric and ferroelectric materials.

and characterization. The thesis is organized as follows. This chapter gives a brief background to the concept of ferroelectricity and introduces $Ba_xSr_{1-x}TiO_3$ (BSTO), the ferroelectric material system under consideration in this thesis. Chapter 2 gives an introduction to BSTO thin film technologies and summarizes some results on laser ablated BSTO thin films characterized using parallel plate varactor structures. Chapter 3 constitutes the core of the thesis and discusses the actual BSTO TFBAR studies. Chapter 4 discusses preliminary results of a fabricated switchable ladder filter based on BSTO TFBARs. A brief summary and concluding remarks are given in Chapter 5.

1.2 Ferroelectricity and related properties

In this section a brief introduction to the concept of ferroelectricity is given. The relation between ferroelectrics, ordinary dielectrics, piezoelectrics and pyroelectrics is described.

Fig. 1.1 schematically shows how the general class of dielectrics (insulators) can be divided into subgroups of piezoelectric, pyroelectric and ferroelectric materials. From symmetry considerations all possible crystal structures can be divided into 32 crystal classes or crystallographic point groups. Out of these 32 crystal classes 11 are centrosymmetric, i.e. they contain a center of inversion symmetry which inhibits the crystal from having polar properties.

The remaining 21 crystal classes are all non-symmetric, allowing the crystal to contain one or more polar axes. All but one of the non-symmetric crystal classes exhibit the *piezoelectric effect*, i.e. a coupling between the electrical and mechanical systems which allows electrical energy to be transformed to mechanical energy and vice versa. In piezoelectric materials an applied mechanical stress results in polarization charges at the crystal surfaces (direct piezoelectric effect) and an applied electric field causes the material to change its shape (converse piezoelectric effect). Piezoelectricity is linear, if the sign of the applied field is reversed the response is also reversed. Centrosymmetric materials also

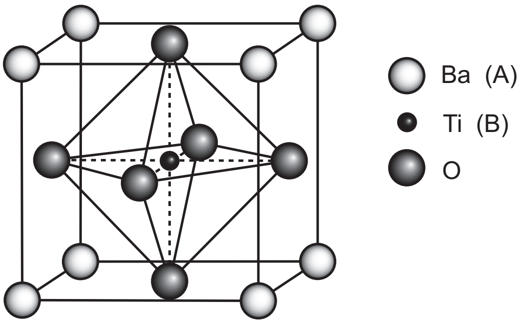

Fig. 1.2: Cubic $BaTiO_3$ unit cell. (General perovskite, ABO_3.)

change their shape slightly as an electric field is applied through the effect known as *electrostriction*, present in all dielectrics. In contrast to the converse piezoelectric effect electrostriction is quadratic with the applied field, or more correctly with the induced polarization [1], i.e. reversing the field results in the same mechanical response. The electrostrictive effect is very weak for most materials but can in some cases, such as $Ba_xSr_{1-x}TiO_3$, be considerable, as will be discussed in chapter 3.

10 of the 20 piezoelectric crystal classes reveal a spontaneous polarization in absence of an external electric field. The spontaneous polarization charges on the crystal surface change with temperature and the group of crystals are said to exhibit the *pyroelectric effect*. If in addition the direction of the spontaneous polarization can be switched by an external electric field, the crystal is said to be *ferroelectric*.

1.3 $Ba_xSr_{1-x}TiO_3$

One of the most well known ferroelectric materials is $BaTiO_3$. $BaTiO_3$ crystallizes in the perovskite structure and undergoes a series of phase transitions with increasing temperature, from rhombohedric to orthorhombic to tetragonal structures, all of which are ferroelectric. Above 120°C [2] the material enters a centrosymmetric, non-ferroelectric cubic phase, referred to as the *paraelectric* phase. Fig. 1.2 shows the cubic $BaTiO_3$ unit cell. The Ti ion in the center of the unit cell is too small to completely fill the space created by the Ba-O ions, and hence is easily displaced from the center, leading to a high permittivity. The lower symmetry phases can be seen as an attempt to minimize the size of the Ti cavity, resulting in a displacement of the Ti ion and thus a net polarization [3].

For applications in tunable microwave devices the paraelectric phase is generally of most interest. This phase reveals strongly field dependent properties (e.g. relative permittivity) without the additional loss mechanisms and hysteresis effects present in ferroelectric phases. As mentioned above, the transition temperature, or Curie temperature, from the cubic paraelectric phase to the ferroelectric tetragonal phase is 120°C for $BaTiO_3$, and the material is thus ferroelectric at room temperature. To lower the Curie temperature $BaTiO_3$ can be combined in a solid solution with $SrTiO_3$, which is a so-called incipient ferroelectric, also with the perovskite crystal structure. Incipient ferroelectrics, or quantum paraelectrics, are materials whose properties resemble those of a ferroelectric in the paraelectric phase, but never reaches a ferroelectric phase transition even at very low temperatures. $SrTiO_3$ is cubic and centrosymmetric at room temperature and undergoes a structural phase transition with reducing temperature to a tetragonal phase at 105K [2]. In contrast to the tetragonal phase of $BaTiO_3$, this phase is however still centrosymmetric, and the material is paraelectric for all temperatures. $BaTiO_3$ and $SrTiO_3$ form a solid solution $Ba_xSr_{1-x}TiO_3$ (BSTO) for all compositions x, and the Curie temperature decreases almost linearly with increasing Sr concentration [4]. This is very useful from an application point of view since important material parameters such as permittivity, which are strongly dependent on the Curie temperature, can be tailored in a wide range by choosing a material with the appropriate composition x. It can be noted that BSTO above the Curie temperature (in the paraelectric phase) does not exhibit the ferroelectric and piezoelectric properties as discussed above, but is still commonly referred to as a ferroelectric material.

Fig. 1.3 shows the temperature dependence of the relative permittivity for ceramic BSTO with varying Ba/Sr content. The phase transition is accompanied by a dramatic increase of the permittivity. Above and below this peak the material reveals paraelectric and ferroelectric properties, respectively. The shift of the transition temperature with increasing Sr content can be clearly seen, indicating that more than 30% Sr is needed in order for the material to be paraelectric at room temperature. Fig. 1.4 shows schematic dependences of the polarization as a function of electric field. The paraelectric phase presents field dependent properties (e.g. permittivity, slope of the P-E plot) allowing tunability, but is free of hysteresis.

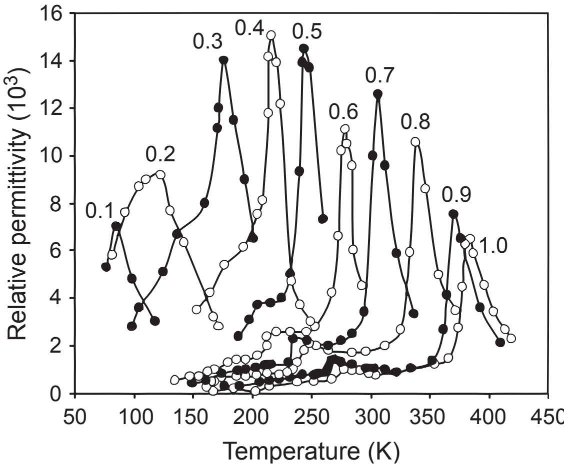

Fig. 1.3: Relative permittivity of ceramic $Ba_xSr_{1-x}TiO_3$ as a function of temperature, for different Ba concentration x. From [5].

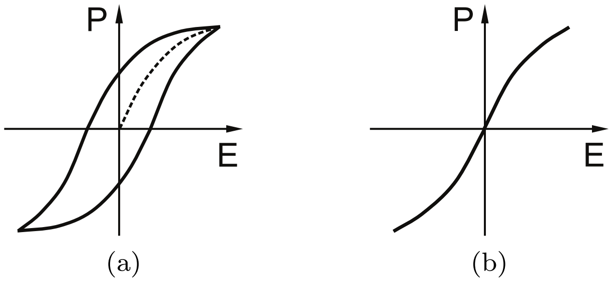

(a) (b)

Fig. 1.4: Schematic representation of polarization as a function of electric field for material in ferroelectric phase (a) and paraelectric phase (b).

Chapter 2

Ferroelectric thin films

Ferroelectric ceramics have been used for high density capacitors and piezoelectric transducers since the 1940s [6]. Since then tunable high frequency devices have been demonstrated using both bulk ferroelectric ceramics and single crystals, as well as thick ceramic films including HTCC and LTCC technologies [7]. Inspired by the integrated circuit development, thin film materials emerged during the 1970s and 1980s [6] and have been extensively studied until today, aiming at non-volatile memory applications [8], sensors and actuators [9, 10], as well as tunable microwave components [7]. The electric fields required to obtain appreciable tuning is easily achieved at relatively low bias voltages with material in thin film form, and possibilities for small size, silicon integrated components are attractive.

2.1 Thin film technologies

Several thin film deposition technologies have been used and reported in the literature for the synthesis of ferroelectric films. Brief descriptions of the most common and successful methods are given below.

MOCVD (Metalorganic chemical vapor deposition), originally developed for epitaxial growth of compound semiconductor materials, is a growth technique capable of producing high quality thin films of various materials including metals and ferroelectrics [11]. Complex metalorganic source materials, precursors, are introduced into the growth chamber in gas form and react on a heated substrate to form the solid thin film. Growth rate and composition are controlled by adjusting the mass flow rate of the different gases. MOCVD has been shown to be able to produce $\mathrm{Ba}_x\mathrm{Sr}_{1-x}\mathrm{TiO}_3$ films with very good composition control, uniform large area coverage, and beneficial columnar microstructure [7]. Examples of precursors for growth of $\mathrm{Ba}_x\mathrm{Sr}_{1-x}\mathrm{TiO}_3$ films are $\mathrm{Ti(OPr)_2(thd)_2}$, $\mathrm{Ba(thd)_2}$, $\mathrm{Sr(thd)_2}$, where Pr=propyl and thd=2,2,6,6-tetramethyl-3,5-heptanedionate [11].

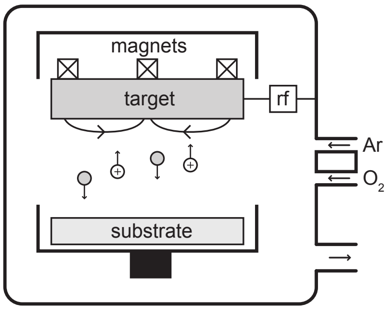

Fig. 2.1: Schematic of magnetron sputtering system.

Metalorganic decomposition (MOD) and *sol-gel* are related low investment cost techniques based on direct application of the precursors on the wafer by spin coating, spraying or dipping. Subsequent high-temperature treatment decomposes the host compound and leaves the solid film on the substrate [11]. The desired film thickness is obtained by repeated application of precursor layers. Sol-gel synthesized films often reveal a granular microstructure although columnar growth can also be achieved [7].

MOCVD and MOD/sol-gel are chemical deposition methods relying on decomposition of volatile precursor materials on a heated substrate to form the solid film. Physical deposition methods on the other hand are based on condensed phase source materials being sputtered, evaporated or by other physical means transferred to the substrate.

Magnetron sputtering is one of the most widely used physical methods for deposition of ferroelectric films, see Fig. 2.1. In the general sputtering process an inert gas, usually Ar, is introduced in the growth chamber. A plasma discharge is ignited by dc or rf power applied to the target material (the cathode), accelerating Ar^+ ions towards the target, while accelerated secondary electrons maintain the discharge by continuously ionizing more species of the sputter gas. The ion bombardment of the target material leads to mainly neutral target atoms being ejected and deposited on the substrate. In a magnetron sputtering setup magnetic fields confine the secondary electrons to a "racetrack" region close to the target, improving the ionization efficiency and allowing operation at lower voltage and pressure. Magnetron sputtering of $Ba_xSr_{1-x}TiO_3$ is performed with a stoichiometric target, rf power, and reactive oxygen gas introduced in addition to the inert Ar working gas in order to minimize oxygen deficiency in the ferroelectric film.[7, 11]

Laser ablation, or *pulsed laser deposition (PLD)*, is another physical deposition method based on high energy laser pulses ejecting material from a ceramic target. The resulting highly directional plume of neutral atoms, molecules, ions, electrons, and larger clusters and droplets expands through either vacuum or an ambient gas and forms a thin film on the substrate surface, see Fig. 2.2 [11]. PLD is suitable for complex oxide

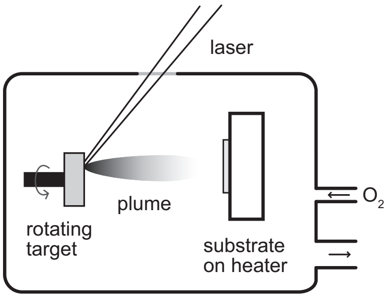

Fig. 2.2: Schematic of laser ablation system.

materials such as high temperature superconductors and ferroelectrics due to the highly stoichiometric transport of material from the target to the substrate surface. The relative simplicity of the system combined with possibilities to vary the growth parameters in a wide range, and to share one laser between several growth chambers, makes laser ablation suitable for research environments for synthesis of complex or novel materials and multilayers. A disadvantage of the conventional PLD technique is the limited size of substrates. Special arrangements using scanning of the laser beam and rotation/translation of the substrate have however been developed allowing large area depositions [7]. Depending on deposition conditions and choice of substrate material, magnetron sputtering and laser ablation can produce ferroelectric films with various microstructure, ranging from high quality epitaxial and textured columnar films to amorphous films.

Irrespective of deposition technology some differences are observed when comparing the properties of thin films with their bulk material ceramic or single crystal counterparts. Most markedly the strong peak in the permittivity accompanying the ferroelectric phase transition (Fig. 1.3) is for thin film materials generally severely damped, and shifted towards lower temperatures. The resulting overall permittivity reduction, the strength of which depends on the film thickness, is typical for thin film ferroelectrics. Higher dielectric losses due to film imperfections, oxygen vacancies, grain boundaries, etc. are also characteristic of many films. This degradation of material properties of course sets a limit to the performance of thin film devices and the origin and processes behind it is therefore of highest interest.

2.2 Laser ablated ferroelectric films

In this work BSTO films have been grown by PLD on metalized high resistivity Si substrates. In this section some general results from these films are discussed, as characterized using parallel plate varactor test structures.

For parallel plate structures the bottom electrode is crucial since it forms the template for the BSTO film growth. The generally accepted electrode material of choice for growth of BSTO films is Pt, which is sufficiently inert in order to withstand the high temperature oxidizing conditions. Pt electrodes also promote low leakage currents through the ferroelectric film under dc bias. This effect can be explained by the general model of BSTO as a wide band gap semiconductor/dielectric with low carrier concentration [12]. In such a system barriers are formed at the metal/BSTO interfaces, and the barrier height is mainly determined by the work function of the contacting metal. High work function Pt at the cathode would thus result in a high barrier to charge injection, and low leakage currents, while lower work function metals such as Ti or Al would be less favourable in this respect. This is in line with qualitative observations made for various contact metals throughout this work. Conductive oxide electrodes such as $SrRuO_3$, which may have microstructural advantages over metal electrodes, are generally considered not to be an option for room temperature high frequency applications due to their limited conductivity and lower barrier to charge injection.

In this work growth of BSTO thin films have been carried out in two different PLD systems, both equipped with a KrF excimer laser emitting 248 nm wavelength 30 ns pulses. The laser pulses are focused into a 1×4 mm^2 spot on a rotating 12 mm diameter ceramic target, ablating material onto the heated substrate in an on-axis configuration. O_2 is used as reactive gas during all depositions.

The ferroelectric film microstructure has been studied using scanning electron microscopy (SEM), atomic force microscopy (AFM) and X-ray diffraction (XRD). A typical SEM cross section image can be seen in Fig. 2.3a, revealing a pronounced columnar structure with grains extending through the film thickness. The lateral size of these columns can be estimated from AFM images of the film surface, Fig. 2.3b, to be approximately 30 nm (confirmed by TEM studies [13]). XRD θ-2θ scans, Fig. 2.4, show a mixed phase content of the ferroelectric film. (100) and (110) phases are clearly present, while a possible (111) phase is masked by strong reflections from thick (111) textured Au electrodes.

Below results from $BaTiO_3$ based parallel plate varactor test structures will be discussed, emphasizing how the PLD growth parameters affect the properties of the resulting film, and highlighting a few general ferroelectric thin film characteristics. The varactors are fabricated on platinized high resistivity Si substrates, with evaporated Au/Pt (500/50 nm) bottom and top electrodes sandwiching the ferroelectric film. The thick Au layers minimize the electrode related losses at higher frequencies [14]. The top electrode (1, Fig. 2.5) consists of a circular patch, 30 µm or 10 µm in diameter, while the non-patterned bottom electrode (2, Fig. 2.5) is capacitively contacted through a large area top electrode, effectively creating a parallel plate capacitor suitable for measurements with ground-signal-ground microprobes. This simple de-

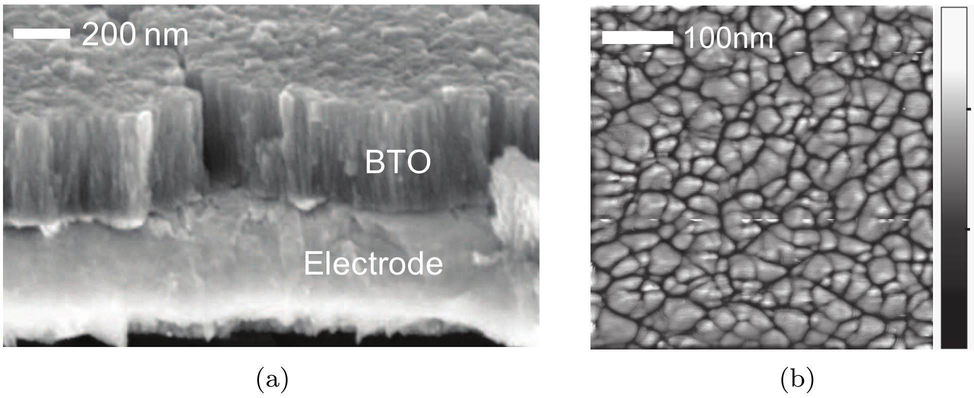

Fig. 2.3: Typical SEM cross section image (a) and AFM surface image (b) of $BaTiO_3$ films.

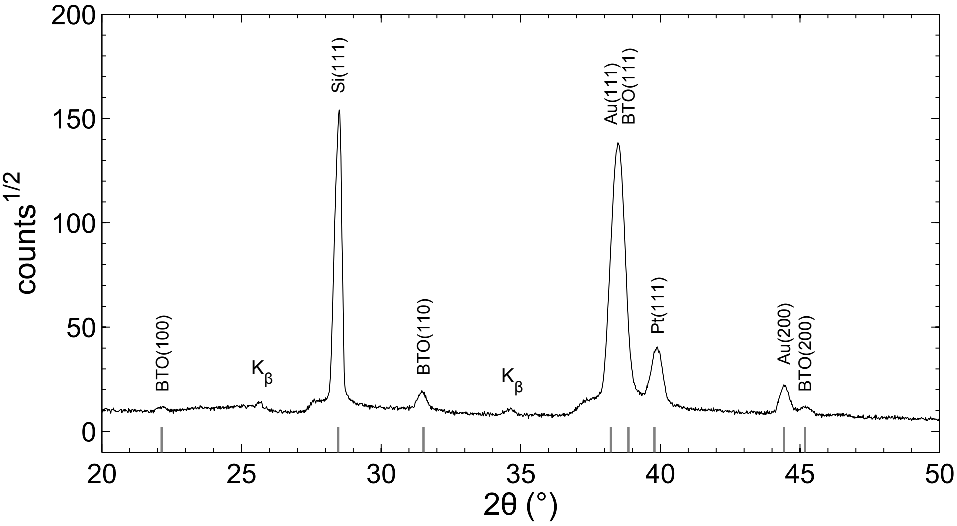

Fig. 2.4: XRD θ-2θ data for $BaTiO_3$ varactor structure on Si(111) substrate with Au/Pt electrodes. Peak positions calculated from reference data are marked along the horizontal axis.

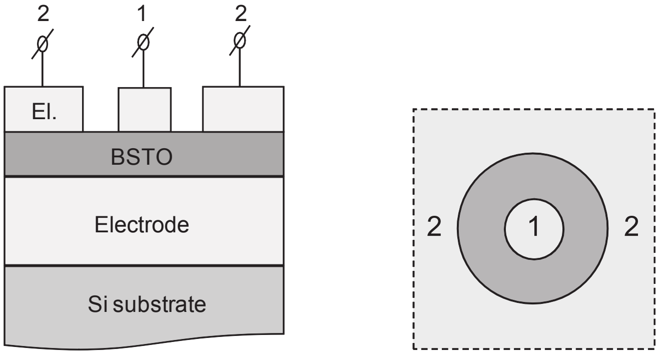

(a) (b)

Fig. 2.5: Schematic cross section (a) and top view (b) of circular varactor test structure used for ferroelectric film characterization.

sign minimizes the impact of electrode parasitics and requires only one lithography step, allowing relatively quick ferroelectric film characterization. Two important PLD growth parameters have been studied using these varactor structures; the substrate temperature and the oxygen pressure during deposition.

2.2.1 Impact of substrate temperature

Fig. 2.6a shows the temperature dependence of the apparent permittivity, ϵ_a, for a set of $BaTiO_3$ films grown at different substrate temperatures, reported in Paper [F]. ϵ_a is calculated from the measured parallel plate capacitance, C, at 1 MHz frequency as

$$\epsilon_a = \frac{Ct}{\epsilon_0 A}, \tag{2.1}$$

where t is the film thickness and A is the area of the top electrode. The permittivity is seen to be strongly dependent on the ferroelectric film growth temperature, with a maximum permittivity of approximately 900. These results are in line with the thin film effects discussed above. Compared to the data for bulk $BaTiO_3$ in Fig. 1.3 the peak in the permittivity is very broad, shifted towards lower temperatures, and the permittivity maximum is almost ten times lower. Reducing the growth temperature results in properties even further from the bulk material counterpart. A positive side effect is that the temperature stability, which is an issue of concern for bulk ferroelectrics due to the very sharp temperature dependence of the permittivity, can be seen to be dramatically improved for the thin films in general, and with decreasing growth temperature in particular.

Fig. 2.6b shows the room temperature dc field dependence of the permittivity for the same set of samples. Almost hysteresis free symmetrical

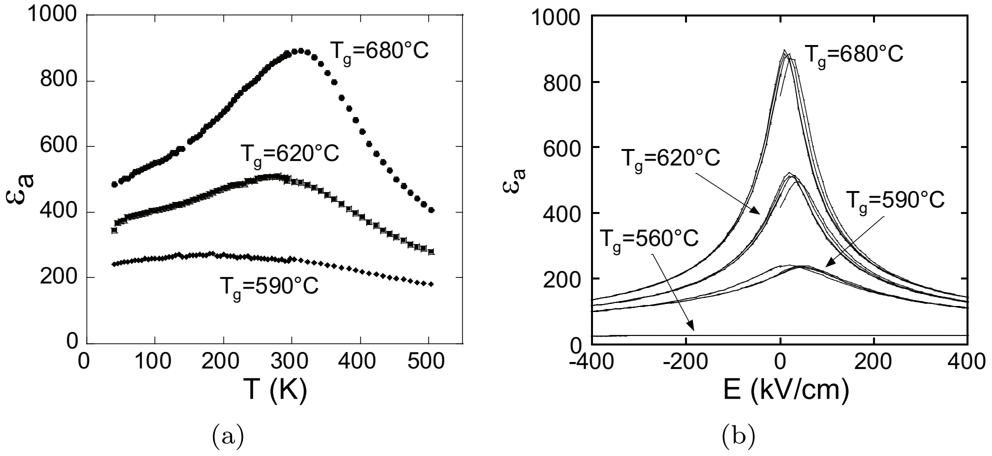

(a) (b)

Fig. 2.6: Temperature dependence (a) and dc field dependence (b) of the relative permittivity in $BaTiO_3$ films grown at different substrate temperatures, T_g.

response is observed, indicating close to paraelectric type performance. This is supported by the fact that the ferroelectric phase transition for non-perfect crystals occurs at a slightly lower temperature than the permittivity maximum [15]. These measurements reveal one of the most important characteristics for a tunable material, the relative tunability (here permittivity tunability), defined as

$$T(E) = \frac{\epsilon(0) - \epsilon(E)}{\epsilon(0)} 100\% \qquad (2.2)$$

for some bias field E. The permittivity tunability is more than 80% for the film grown at the highest temperature and is decreasing with growth temperature. This demonstrates a general trend – the higher the zero bias permittivity, the higher the tunability, for a given bias field [5].

Fig. 2.7 shows the measured loss tangent for two samples grown at different temperatures in the frequency range 1–25 GHz. The capacitance (not shown) is in principle independent of the frequency in the whole range, with tuning characteristics comparable to those measured at 1 MHz. Contributions to the varactor loss tangent at microwave frequencies can be roughly divided into three main categories: i) Intrinsic dielectric losses in the ferroelectric film due to ac field – phonon interactions, ii) extrinsic losses in the film originating from microstructural/interfacial defects, and iii) losses due to the finite conductivity of the metal electrodes. Intrinsic losses represent the fundamentally lowest limit, and in practice the loss level of thin films is usually dominated by extrinsic mechanisms. Losses due to charged defects, often identified as oxygen vacancies, are considered to contribute significantly to the extrinsic losses in ferroelectric films at microwave

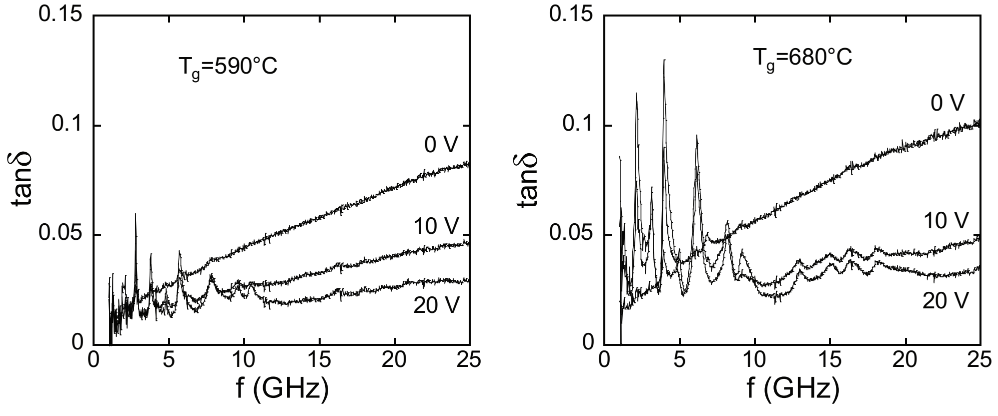

(a) (b)

Fig. 2.7: Loss tangent as a function of frequency, with dc bias voltage as parameter, for $BaTiO_3$ films grown at 590°C (a) and 680°C (b).

frequencies [5, 16]. This loss mechanism has an approximate functional dependence $\tan\delta_{ch} \propto \epsilon\omega$ [5], and the results presented in Fig. 2.7 can be seen to be in qualitative agreement with this dependence. Reducing the permittivity of the films, either by growth temperature or by bias field, results in a reduction in the loss tangent. Losses due to series resistance of electrodes would in principle reveal a similar bias dependence ($\propto \omega R_S C(E)$) but this contribution can be considered small for the type of test structure and electrodes used for these measurements [16]. An additional effect, resonant acoustic absorption of the microwave energy, is the origin of the peaks in the losses observed under bias below 10 GHz. The electro-acoustic properties of BSTO films will be covered in chapter 3.

In summary the study of $BaTiO_3$ samples prepared at different substrate temperatures reveal that a higher growth temperature leads to more bulk-like properties in terms of permittivity and tunability. The dielectric losses however decrease with bias field for all films, indicating that an extrinsic loss mechanism is still dominant [17].

In Paper [F] an attempt was made to explain the observed differences in film permittivity as due to a change in the grain size with growth temperature. The grain size (column width) distribution of each sample could due to the known columnar structure be estimated using analysis of AFM images of the film surfaces. A clear trend was observed with a mean grain diameter increasing with growth temperature from 25 nm to 35 nm over the studied interval (560°C to 680°C). A model assuming the film to consist of grain cores with bulk-like properties surrounded by amorphous low permittivity grain boundary regions was successful in describing the room temperature permittivity variations, but not the overall permittivity behavior over a wide temperature range (shift in the apparent Curie temperature). The commonly referred series capacitor model, or dead layer model, assuming instead a layer of low permittivity material in series with a more bulk-like part of the film, was found to be able to qualitatively explain these effects. No microstructurally distinct layer was however observed in series with the columnar grains in these films.

The series capacitor model can be used to reproduce the commonly observed thickness dependence of ferroelectric thin film properties, and has been the subject of extensive research, without reaching a universally accepted explanation. Several proposed mechanisms, apart from a microstructurally distinct true dead layer, have been found to result in series capacitance type behavior, including Schottky barrier depletion regions at the film/electrode interfaces [18], space charge within non-ideal electrodes [19], interfacial discontinuities affecting the polarization state [15], strain gradients [20], etc. It can be added that measurements on lamellae as thin as 75 nm, produced from single crystal $BaTiO_3$ using focused ion beam etching, have shown bulk-like properties, indicating that the thickness degradation of thin films in principle can be avoided [21, 22].

2.2.2 Impact of oxygen pressure

An important growth parameter in the PLD process, apart from the substrate temperature, is the amount of reactive O_2 gas in the chamber during deposition. Fig. 2.8 shows the room temperature zero bias permittivity as a function of the O_2 pressure for a series of $BaTiO_3$ films grown at 650°C, revealing a maximum at 0.2 mbar. Changes in the film stoichiometry is the most probable reason for this strong dependence. Several studies have shown that a proper Ba/Ti or (Ba+Sr)/Ti ratio of the film is critical in order to reach a high permittivity [23, 24]. Specifically, data of $BaTiO_3$ film permittivity as a function of PLD pressure, qualitatively in agreement with the data in Fig. 2.8, can be found in Ref. [25].

Similarly to the growth temperature studies, the films with the highest permittivity were found to consist of the largest grains. SEM images of the surfaces of $BaTiO_3$ films grown at 0.2 mbar and 0.4 mbar O_2 pressure are shown in Fig. 2.9. The larger grains can be explained by more energetic plume species reaching the substrate due to fewer collisions with gas molecules.

The film with the highest permittivity also shows higher tunability, as expected, and higher losses. Most importantly for this work however is that the microwave response for the film grown at 0.2 mbar O_2 reveals the most pronounced electro-acoustic effects, see Fig. 2.10. These effects, which are problematic for parallel plate varactor applications due to the associated high loss tangent peaks, form the basis for the acoustic resonators discussed in the next chapter.

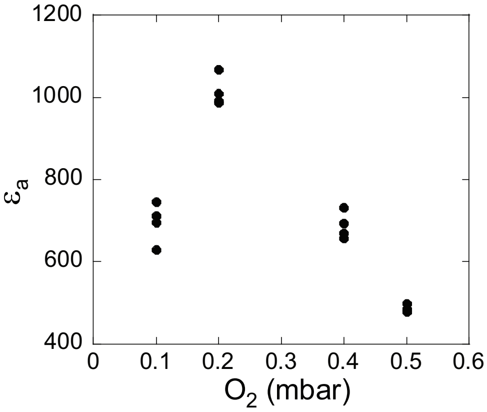

Fig. 2.8: Relative apparent permittivity as a function of oxygen pressure during $BaTiO_3$ film growth.

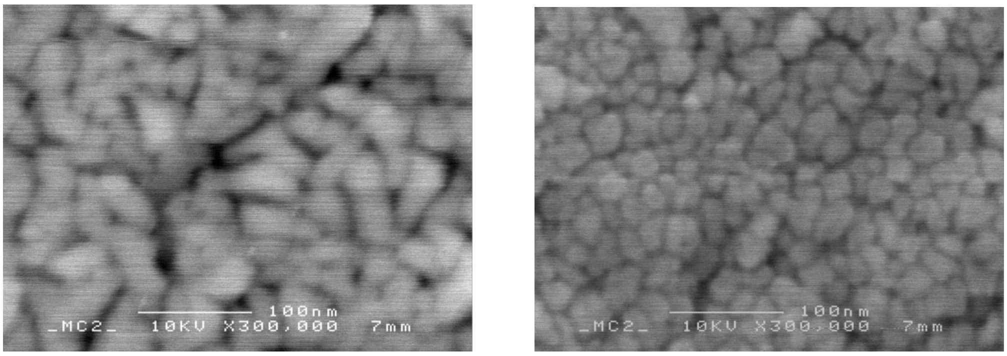

(a)

(b)

Fig. 2.9: SEM images of $BaTiO_3$ films grown by laser ablation at (a) 0.2 mbar O_2, and (b) 0.4 mbar O_2.

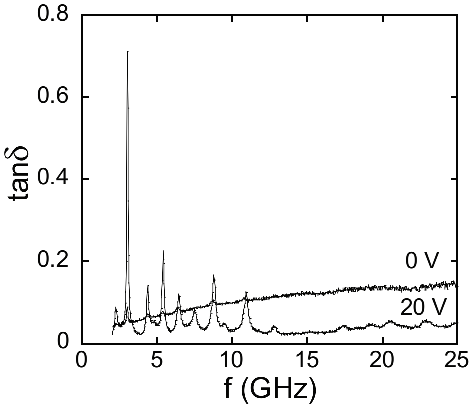

Fig. 2.10: Loss tangent as a function of frequency for $BaTiO_3$ film grown at 0.2 mbar O_2.

In summary the PLD results presented in the previous sections show that the dielectric properties of the ferroelectric film depend strongly on the growth parameters. The highest permittivity and tunability is obtained at a high growth temperature and O_2 pressure close to 0.2 mbar. These results were obtained using a $BaTiO_3$ target. It should be noted however that most of the results are qualitatively representative also for $Ba_{0.25}Sr_{0.75}TiO_3$ films, which are the main focus of the following chapters. Similar dependencies on substrate temperature and O_2 pressure during PLD have been observed for $Ba_{0.25}Sr_{0.75}TiO_3$ films during this work.

Chapter 3

Tunable thin film bulk acoustic wave resonators

3.1 Introduction

Resonators are key components in a multitude of frequency generating and frequency selective components such as oscillators and various types of filters. Applications range from radio communication systems to wrist watches to sensors, and piezoelectric crystals have been extensively used as the resonant element. An ac electric field applied to a piezoelectric crystal excites acoustic waves which result in a resonance at a frequency determined by the mechanical properties and physical dimensions of the crystal. Since the resonance frequency of piezoelectric resonators based on bulk acoustic waves depend on the crystal dimensions, the upper possible frequency of operation is mainly determined by the thickness of the piezoelectric crystal plate. For the conventional approach, cleaving of bulk material into thinner crystals, the maximum frequency is generally below a few hundred MHz. Applications in e.g. wireless communication systems require small size, high Q-factor resonators for frequency generation and filtering in the microwave frequency regime. This need has been the driving force for the thin film bulk acoustic wave resonator (TFBAR) technology, based on piezoelectric materials in thin film form, which allows fabrication of electro-acoustic resonators operating at several GHz.

The principal TFBAR structure consists of a piezoelectric film sandwiched between two electrodes. As an ac electric field is applied, acoustic waves are generated due to the converse piezoelectric effect and reflected within the piezoelectric film. At the frequency where half the acoustic wavelength is equal to the piezoelectric film thickness a mechanical standing wave is formed. The acoustic waves in turn polarize the material through the direct piezoelectric effect. For longitudinal excitation resonators like normal TFBARs, the mechanically induced polarization at the standing wave frequency is 180° out of phase with the dielectric polarization due to the externally applied ac field. At this frequency the net polarization charge, and thus current, is minimized, giving rise to a parallel type resonance at the electrical port. At a slightly lower frequency the two polarization contributions are in phase, resulting in a high current and a series resonance. Mechanical loading of finite thickness electrodes and other layers in the real resonator stack results in deviations from this ideal case which assumes perfect boundary conditions. The resonances e.g. often occur at frequencies considerably lower than what is predicted by the standing wave criterion above. The description is however quite instructive and qualitatively explains the occurrence of the series and parallel resonances as well as their strong dependence on piezoelectric film thickness.

Practical thin film resonator designs roughly fall into two main categories depending on how the necessary acoustic isolation from the thick substrate material is provided, see Fig. 3.1. The first approach involves removal of material below the active resonator area, forming a free-standing membrane structure, Fig. 3.1a, either by etching of the substrate from the backside or by using a sacrificial layer forming an air bridge structure. Acoustically this design is close to ideal, with low impedance air providing a high reflection coefficient and effective concentration of the acoustic energy to the piezoelectric film. The second approach is based on a multilayer acoustic mirror or Bragg reflector structure substituting for the free surface at the bottom, Fig. 3.1b.

A comment on terminology should be made. Often in the literature membrane based resonators are referred to as TFBARs or FBARs while reflector based resonators are distinguished as solidly mounted resonators (SMRs). In this work no such distinction is made and the term TFBAR is applied for both types. From the authors point of view the term TFBAR describes the type of component quite clearly (resonator, bulk acoustic wave, thin film technology), while implying nothing, except by convention, about how acoustic isolation is obtained. If a distinction between the two main resonator types is needed in this work, the terms membrane type TFBAR and solidly mounted TFBAR are used.

Currently the commercialized TFBAR technology is based on AlN as the piezoelectric active layer and both membrane and solidly mounted designs. AlN has been successful due to its low acoustic losses and sufficiently high electromechanical coupling coefficient. The breakthrough application was the introduction of a duplexer filter for the 1900 MHz US-PCS band in 2001, where extremely compact TFBAR technology could replace a bulky ceramic duplexer [26]. Today TFBAR technology is provided by several manufacturers and widely used for filtering applications in mass market applications such as mobile phones and GPS handsets [27, 28, 29, 30].

Combining the many attractive properties of these conventional TF-

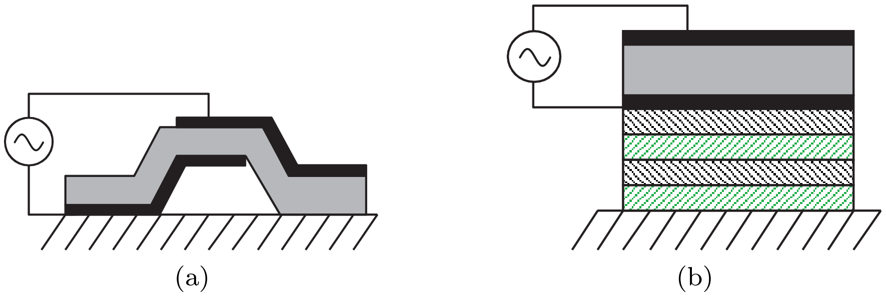

Fig. 3.1: Schematic of membrane type resonator (a) and solidly mounted resonator (b).

BARs with *tunability*, i.e. a possibility to shift the resonance frequency, would enable development of a whole new range of compact components with enhanced functionalities such as tunable filters, switches, voltage controlled oscillators, etc. Some approaches to realize TFBAR tuning with the conventional materials have been reported. Resonance frequency tunability of AlN and ZnO resonators combined with MEMS structures as tuning elements have been reported to reach 0.39% [31] and 1.47% [32], respectively. Electrostatic tuning of the bulk acoustic resonator itself by applying a dc bias directly over the piezoelectric film is however extremely weak for these materials, with reported tunabilities significantly lower than 1% [32, 33].

Ferroelectric perovskite oxides, which often reveal considerable field dependence of physical properties, are considered as an alternative for TFBARs in order to reach wider tuning ranges. Resonators based on Pb(Zr,Ti)O_3 (PZT) thin films show relatively high tunabilities (>3%) [34], although the inherent hysteresis due to the polar phase of the material might be problematic for practical applications, see Fig. 3.2a. Polar phase material also suffers from loss contributions due to domain wall motions and oscillations [35]. In this thesis practically hysteresis-free (Fig. 3.2b) solidly mounted TFBARs based on paraelectric phase $Ba_xSr_{1-x}TiO_3$ are presented and discussed. These resonators show in principle no piezoelectric activity at zero bias field as can be expected from material in the paraelectric phase. Applying a bias field however induces a piezoelectric effect due to breaking of the centrosymmetry of the paraelectric crystal structure, and distinct field dependent resonances appear. The field induced piezoelectric effect is further discussed in section 3.4.

3.2 Design and fabrication

The resonators considered in this work are implemented on high resistivity Si substrates as solidly mounted devices of the type shown in

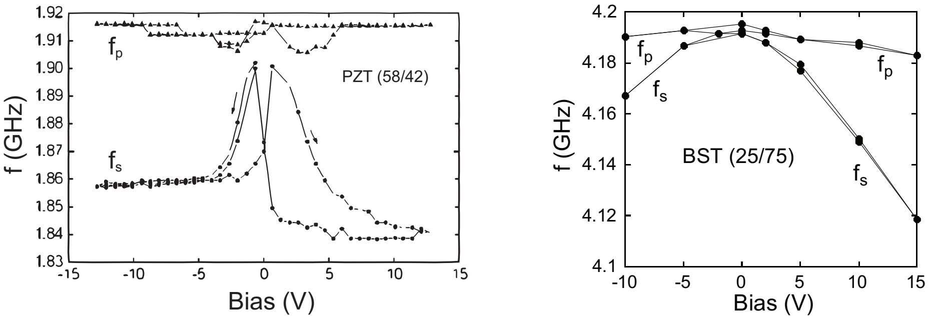

(a) (b)

Fig. 3.2: Resonance frequencies as a function of bias for tunable resonators based on (a) $Pb(Zr_{0.58}Ti_{0.42})O_3$ [34] and (b) $Ba_{0.25}Sr_{0.75}TiO_3$ [this work]. Notice the pronounced hysteresis for the PZT resonator.

Fig. 3.1b. Active layers consisting of either $Ba_{0.25}Sr_{0.75}TiO_3$ or $BaTiO_3$ are deposited by laser ablation as described in section 2.2. The design frequency, 5.25 GHz, was chosen to target future applications in the 5.25 GHz U-NII band and the 5.8 GHz ISM band. Reaching this exact resonance frequency has however not been a primary goal, and the fabricated resonators discussed in this thesis have resonance frequencies in the 3.7–6 GHz range. Two main versions of the tunable resonators have been studied, both of which are designed for on-wafer one-port reflection measurements with ground-signal-ground microprobes. In Paper [E] and Paper [B] resonators consisting of circular structures of the same type as shown in Fig. 2.5 are presented. This design minimizes the fabrication complexity and the impact of electrode parasitics. The main drawback of this layout is the requirement to contact the active resonator area top electrode directly with the microprobe signal pin. This may lead to results which are difficult to repeat and interpret due to scratching of the electrode and possible mechanical loading of the resonator by the probe tip.

In Paper [D] resonators with a more complex design based on patterning of the bottom electrode are introduced, see Fig. 3.3. The idea behind this design is to separate the probe tips from the active resonator area and to evaluate tunable resonators which are possible to incorporate in a circuit application. Conducting layers below the active layer need to be patterned to avoid unwanted capacitive coupling to the top electrode. The active resonator area is defined by the overlap between the top electrode and the bottom electrode which is capacitively coupled to the top electrode ground pads. A second thick metal layer is added to reduce losses due to series resistance of the electrodes. This thick metal does not reach the TFBAR active area in order to keep the mechanical loading of the resonator low. With this design repeated contacting to the same resonator structure is not a problem due to the thick metal

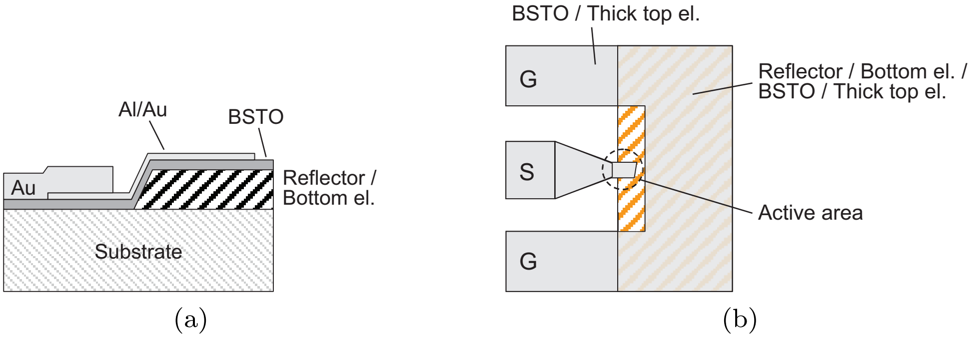

(a) (b)

Fig. 3.3: Schematic cross section (a) and top view (b) of TFBAR with patterned bottom electrode and reflector.

electrode, facilitating e.g. temperature dependence studies, described in section 3.5.

3.2.1 Bragg reflector

Conceptually similar to an optical distributed Bragg reflector, the acoustic reflector consists of pairs of layers with alternating high and low acoustic impedance. The thickness of these layers are specified from the quarter acoustic wavelength in the material at the desired reflector center frequency. The acoustic impedance contrast between the two materials impact on the reflectivity for a given number of pairs, and on the reflector bandwidth. The most widely used material for the low impedance layers is SiO_2 due to its low impedance, low acoustic attenuation, and positive impact on resonance frequency temperature drift [36, 37]. (In contrast to most other materials SiO_2 has a positive temperature coefficient of the elastic constant, allowing temperature compensation [36, 38].) High impedance materials include W, Mo and AlN. W and Mo layers provide high impedance contrast but need to be patterned outside the resonator active area to avoid capacitive coupling with top metal layers, increasing the fabrication complexity.

Au/SiO_2

The resonators presented in Paper [E] and Paper [D] are based on a high impedance contrast Au/SiO_2 Bragg reflector structure providing a wide bandwidth of more than 4 GHz and requiring only two pairs to achieve high reflectivity. Au is generally not considered a suitable material for bulk acoustic wave devices due to relatively high mechanical losses at high frequencies [39]. Technological preferences, oxidation resistance, and possible advantages from incorporating high conductivity material in the reflector stack, effectively making the bottom electrode thicker, however motivated the use of Au for the first experiments. The

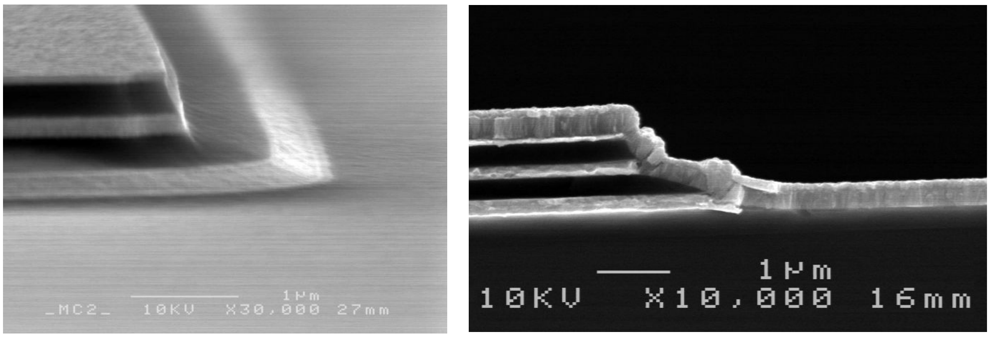

(a) (b)

Fig. 3.4: SEM images of the SiO_2/Au Bragg reflector. (a) Etched step in the reflector and thin bottom electrode. (b) Cross section of the etched step, after deposition of BSTO active layer and top electrode.

SiO_2 (280 nm) and Au (150 nm) layers were deposited in situ using reactive rf magnetron sputtering and dc magnetron sputtering respectively. In order to obtain sufficient adhesion thin Ti layers were sputtered in between each reflector layer.

To be able to use the Au containing reflector in the more complex resonator design (Fig. 3.3) the reflector layers need to be removed from areas outside the active area. This is performed using Ar ion milling at 45° impact angle in order to obtain a sloped sidewall. SEM images of the etched reflector edge is shown in Fig. 3.4. It can be noted from Fig. 3.4b that the approximately 1 µm high step disturbs the BSTO film growth, resulting in a rough region along the reflector edge. The thin top electrode needs to traverse this sloped region leading to two possible loss mechanisms: i) increased series resistance due to the rough topography, and ii) acoustic energy being lost due to acoustic waves being launched in non-vertical directions. In addition, the approach to pattern the bottom electrode in the same ion milling process as the reflector layers results in a resonator design where the Bragg reflector does not extend outside the active area in the etched step region where the top electrode comes in, leading to acoustic losses along approximately 25% of the resonator perimeter where the reflector is not well defined.

HfO_2/SiO_2

Instead of developing the metal-containing Bragg reflector further, focus was shifted towards realizing a fully non-conducting reflector stack. With a non-conducting reflector only the bottom electrode would require patterning, resulting in a considerably smaller step for the active layer and top electrode to cover. The problem with resonator perimeter leakage could also be expected to be less severe since the Bragg reflector extends “infinitely” outside the resonator active area in all directions.

HfO_2 is a dielectric material with sufficiently high acoustic impedance to allow fabrication of a reflector stack using a reasonable number of layers in combination with low impedance SiO_2. In Paper [B] results on resonators based on an all-dielectric HfO_2/SiO_2 reflector are reported. The SiO_2 (284 nm) and HfO_2 (260 nm) layers of the three pair reflector stack is deposited in situ by reactive rf magnetron sputtering from elemental Si and Hf targets.

The reflectivity response of a given Bragg reflector can be estimated by considering the acoustic input impedance of the layered stack below the active layer by iterative use of the transmission line impedance equation

$$Z = Z_i \frac{Z_l + Z_i \tanh \gamma_i t_i}{Z_i + Z_l \tanh \gamma_i t_i} \tag{3.1}$$

where Z_l is the impedance loading the ith layer with impedance Z_i, propagation constant γ_i and thickness t_i. The reflectivity is then given as

$$R = \frac{Z_{BSTO} - Z_{REFL}}{Z_{BSTO} + Z_{REFL}}, \tag{3.2}$$

where Z_{BSTO} is the acoustic impedance of the BSTO active layer and and Z_{REFL} is the input impedance of all the layers below (substrate, reflector, bottom electrode). Fig. 3.5 shows the reflection response as a function of frequency for Bragg reflectors based on HfO_2/SiO_2 (3 pairs) and Au/SiO_2 (2 pairs). It can be noted that the bandwidth for the Au based reflector is slightly wider due to the higher acoustic impedance contrast, but that the center frequency reflectivities are comparable.

3.2.2 Electrodes

The choice of top and bottom electrodes sandwiching the active layer is crucial for obtaining the desired resonator characteristics. From the point of view of resonator Q-factor the electrode resistance may limit the performance, especially at the series resonance where large currents are drawn through the device. Alleviating this by introducing thicker electrodes in the acoustic path however leads to increased mechanical losses, since metals in general have higher acoustic losses than dielectrics. It can be shown that the Q-factor reveals a maximum as a function of electrode thickness due to these effects [26, 40].

The effective resonator coupling coefficient, mirroring the frequency separation between series and parallel resonances, is also dependent on the choice of electrode materials. High impedance electrodes confine the acoustic energy more effectively to the active layer, leading to a higher coupling coefficient. For a given electrode thickness the effec-

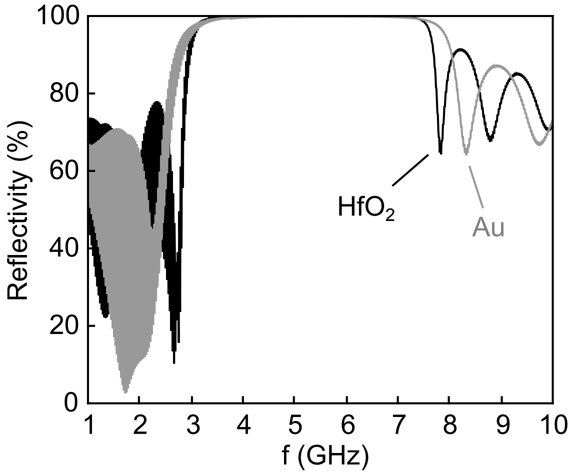

Fig. 3.5: Calculated reflectivity of HfO_2/SiO_2 and Au/SiO_2 Bragg reflectors including a 100 nm Pt bottom electrode.

tive resonator coupling coefficient can even exceed the intrinsic coupling coefficient of the piezoelectric material itself [39]. This effect has been proven crucial for the success of AlN-based resonator filters since the effective coupling coefficient determines the separation between the series and parallel resonances, and thus is directly connected to filter bandwidth. Mobile phone filters require effective coupling coefficients of 6–7%, reached with small margin by AlN based TFBARs [41]. Too thick electrodes lead to a reduction of the effective coupling coefficient (and tunable TFBAR tunability [42]) because a larger portion of the resonator volume is consisting of non-piezoelectric electrode material [39].

An additional factor related to electrode thickness is the mass loading effect of the active layer. Thicker (and more dense) electrodes lead to a lowering of the resonance frequencies. Compensating for this mass loading can be done by using a thinner active layer, which may or may not be desirable depending on the application.

In order to maximize Q-factor and coupling coefficient it seems clear that a low resistivity, high acoustic impedance material is preferable. High impedance electrodes commonly used for AlN TFBARs include Mb and W. If electrode resistance is an issue dual layer electrodes can be used, with a high impedance material in contact with the active layer to maximize the coupling, covered by a second layer of a low resistivity metal such as Al [39].

Top electrode

Throughout this work Al has been used as the main top electrode material. The advantages of Al include its low resistivity and low acoustic impedance. This allows a low electrode resistance without excessive resonator loading. Due to the relatively high frequency the active BSTO layer thickness is already small, in the 200–400 nm range. This low thickness combined with the high dielectric constant of BSTO results in very small resonators in order to reach reasonable impedance levels. Resonator loading should thus be kept as low as possible. No specific goal for the resonator effective coupling coefficient has been pursued and higher impedance top electrodes have not been considered in this work.

Bottom electrode

The choice of bottom electrode is more critical since it also serves as the template on which the BSTO active layer is grown. As mentioned in section 2.2 the generally preferred material for contacting BSTO thin films is Pt due to its inertness and high work function. Au electrodes have also been studied for varactor applications with promising results due to its higher conductivity [43].

The resonators presented in Paper [E] and Paper [D] are based on Au bottom electrodes, deposited in situ with the Au/SiO_2 Bragg reflector.

As the all-dielectric HfO_2/SiO_2 Bragg reflector was introduced, efforts were simultaneously put into developing a Pt bottom electrode. The expected benefit with Pt was the possibility to apply higher dc bias due to the superior properties of the Pt/BSTO interface. Avoiding the poor acoustic performance of Au was also desirable. Adhesion between an inert metal such as Pt and an oxide surface, here the top SiO_2 layer of the reflector stack, is in general very poor. The issue is even more pronounced since the thin Pt electrode needs to be able to withstand the high temperature BSTO film deposition with its accompanying diffusion and thermal strain effects. Adhesion promoting layers and diffusion stop barriers need to be as thin as possible in order not to degrade the acoustic properties of the stack. Several versions of bottom electrode configurations were studied, including Pt, Ti/Pt, TiO_2/Pt, Ti/TiO_2/Pt, TiO_2/Au/Pt, Ti/TiN/Pt, W/Pt, using varying processing conditions. Several of the combinations result in very rough surfaces after high temperature BSTO deposition, most probably due to diffusion of Ti leading to locally reduced adhesion and TiO_x inclusions in the Pt layer [44]. A Ti(20 nm)/TiO_2(25 nm)/Pt(100 nm) electrode was successfully used for the resonators presented in Paper [B]. This electrode is deposited by magnetron sputtering using radiative heating of the substrate during the deposition of the Ti/TiO_2 layers, and results in a relatively smooth surface after BSTO deposition. The key here is the substrate heating, oxidizing also the thin metallic Ti layer during subsequent reactive sputtering of TiO_2. Auger electron spectroscopy of the Pt surface of this electrode structure after annealing in an O_2 atmosphere (BSTO deposition conditions) showed no trace of Ti. The same electrode structure, deposited *without* substrate heating, however

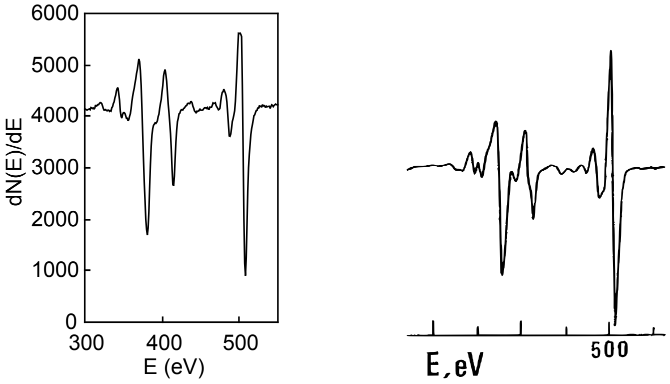

(a) (b)

Fig. 3.6: (a) Auger electron spectroscopy data revealing presence of TiO_2 on the surface of $Ti/TiO_2/Pt$ electrode after annealing in BSTO growth conditions. (b) Reference TiO_2 spectrum from Ref. [45]

show clear evidence of TiO_2 on the surface of Pt after O_2 ambient annealing, see Fig. 3.6, indicating diffusion of Ti through the Pt film and subsequent oxidation at the surface.

For the filter samples, described in chapter 4, a TiO_2/Pt electrode was used.

3.3 Measurement results

Wideband microwave measurements of the fabricated resonators have been performed using HP8510C and Agilent N5230A network analyzers. The resonator structures were contacted using ground-signal-ground microprobes for one-port reflection measurements.

3.3.1 De-embedding procedure

In order to evaluate the resonator itself, without the impact of lead strips and contact resistance, measurements of the resonator test structures of the type shown in Fig. 3.3 are de-embedded using dedicated on-wafer calibration structures, see Fig. 3.7. De-embedding is performed by extracting Y_{TFBAR} from the schematic of Fig. 3.7c. The main impact of this de-embedding is the removal of series inductance due to the lead strips between the active area of the resonator and the contact pads.

Measurements of the circular test structures can be de-embedded by subtracting the series resistance of the electrodes (and the contact resistance), found as the real part of the impedance at the high frequency limit [46]. This gives a closer estimate of the mechanical Q-factor, i.e. an indication of the mechanical properties of the BSTO film itself.

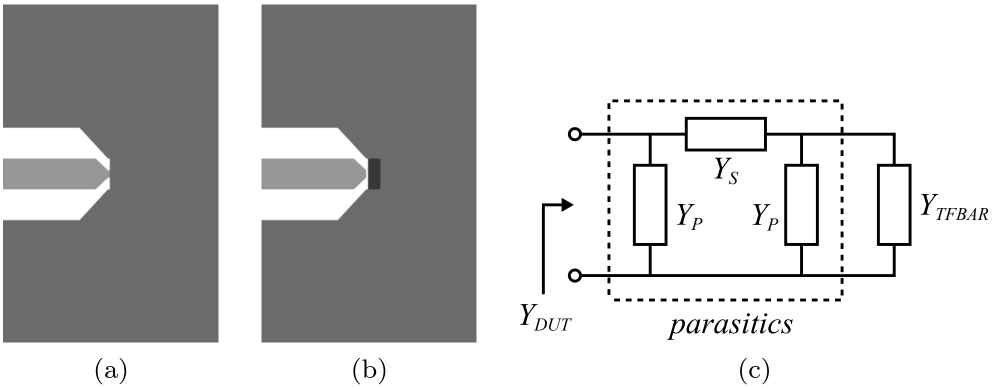

Fig. 3.7: Short (a) and open (b) calibration structures used for resonator measurement de-embedding using the circuit (c).

3.3.2 Resonators with Au/SiO_2 reflector and Au bottom electrode

Fig. 3.8 shows room temperature measurement results, presented in Paper [D], for a resonator of the type shown in Fig. 3.3 based on $Ba_{0.25}Sr_{0.75}TiO_3$, a Au/SiO_2 Bragg reflector and Au bottom electrodes. With no dc bias applied, the response is smooth and the device behaves like a parallel plate capacitor, as expected for BSTO in the paraelectric phase. As dc bias is applied the film becomes piezoelectrically active and the acoustic effects appear, with resonances gradually developing and shifting towards lower frequencies with increasing bias. In agreement with the description of the general TFBAR principle in section 3.1, a series type resonance (minimum impedance) closely followed by a parallel type resonance (maximum impedance), is seen at approximately 4.2 GHz. A clear difference can be noted comparing the wideband frequency response in Fig. 3.8 with the loss tangent measurements for a varactor structure in Fig. 2.7 or Fig. 2.10. The multitude of absorption peaks observed in the varactor case reveals that the layered structure has not been designed with acoustic phenomena in mind. In contrast the TFBAR measurements show a single well defined resonance response due to the acoustically appropriate layer thicknesses and materials. The electro-acoustic effects in varactors are further discussed in Paper [C]. Measurements of the basic circular resonator structures presented in Paper [E] reveal qualitatively similar results.

Fig. 3.9 shows the series and parallel resonances, f_s and f_p, normalized to the (vanishing) zero bias value, and the effective coupling coefficient k_t^2, as a function of dc bias voltage. Results for resonators based on both $Ba_{0.25}Sr_{0.75}TiO_3$ and $BaTiO_3$ are included. The coupling

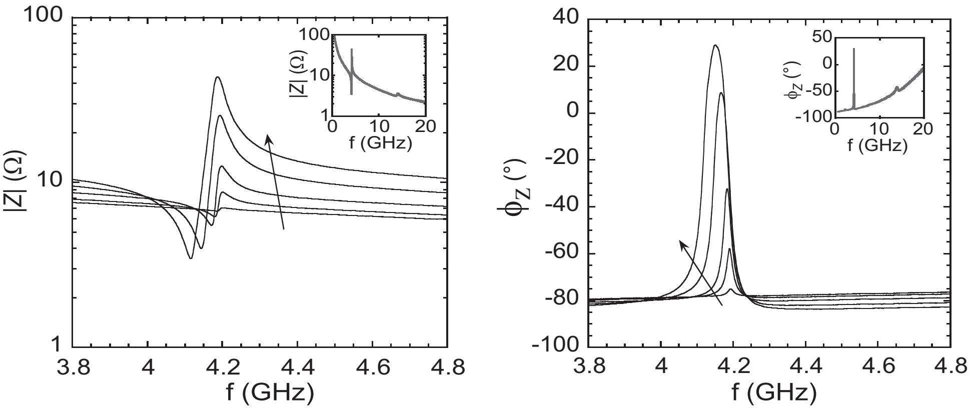

(a) (b)

Fig. 3.8: Measured magnitude (a) and phase (b) of a $Ba_{0.25}Sr_{0.75}TiO_3$ resonator input impedance. Au/SiO_2 Bragg reflector and Au bottom electrode. Arrows indicate increasing dc bias voltage 0, 2, 5, 10, and 15 V. Insets: 0.5–20 GHz, 15 V.

coefficient is computed as [47]

$$k_t^2 = \frac{\pi}{2}\frac{f_s}{f_p}\cot\left(\frac{\pi}{2}\frac{f_s}{f_p}\right). \tag{3.3}$$

In the $Ba_{0.25}Sr_{0.75}TiO_3$ case the series resonance tunability reaches 1.7% at 15 V dc bias and the resonances are tuned towards lower frequencies, with a maximum effective coupling coefficient k_t^2 of 3.7%. In principle no hysteresis is visible as the bias is swept 0V → 15V → 0V. In the $BaTiO_3$ case the resonances are in contrary shifted towards higher frequencies with increasing bias, with a series resonance tunability of 1.3% and a parallel resonance tunability of 3.3%. The coupling coefficient reaches 5.5% at 15 V bias and a marked hysteresis is observed. The resonator Q-factor is estimated as [47]

$$Q = \frac{f}{2}\left|\frac{d\phi_Z}{df}\right|_{f=f_{\mathrm{res}}}, \tag{3.4}$$

where ϕ_Z is the phase of the input impedance and f_{res} is the resonance frequency. The Q-factor reaches a value slightly above 100 for both resonances above 2 V bias for the $Ba_{0.25}Sr_{0.75}TiO_3$ resonator. The Q-factor for the $BaTiO_3$ TFBAR is lower, around 50 for the higher bias points.

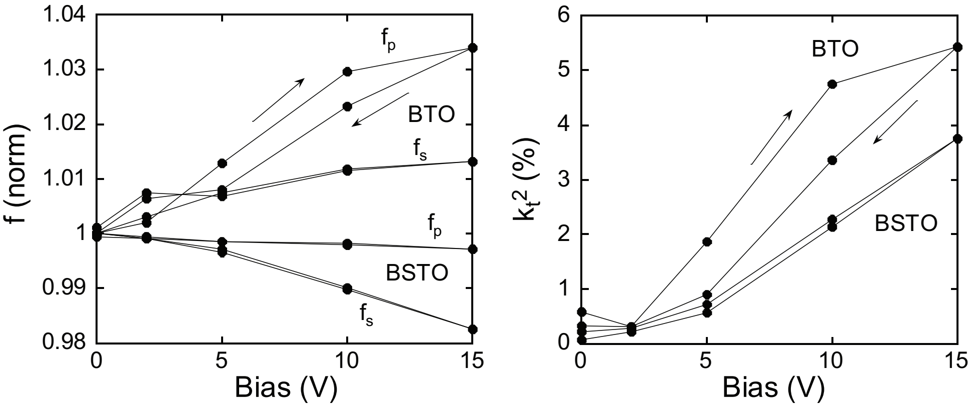

(a) (b)

Fig. 3.9: Series and parallel resonances (normalized) (a) and effective coupling coefficient (b) as a function of dc bias voltage for $Ba_{0.25}Sr_{0.75}TiO_3$ and $BaTiO_3$ resonators. Au/SiO_2 Bragg reflector and Au bottom electrode.

3.3.3 Resonators with HfO_2/SiO_2 reflector and Pt bottom electrode

Fig. 3.10 and Fig. 3.11 show corresponding results, presented in Paper [B], for a $Ba_{0.25}Sr_{0.75}TiO_3$ resonator based on a HfO_2/SiO_2 Bragg reflector and a Pt bottom electrode. The main observation is that the maximum allowed dc bias is considerably increased, in line with the expected improvements from using a Pt electrode. Up to approximately 25 V dc bias can be applied without device damage, compared to approximately 15 V for the version with Au bottom electrode. This in turn leads to a considerably higher maximum tunability (3.8%, series resonance) and effective electromechanical coupling coefficient (7.1%). The active layer for this resonator is thinner, resulting in a higher resonance frequency, approximately 5.7 GHz, and making the difference in device breakdown field between the Au and Pt electrode versions even higher. The Q-factor of the all-dielectric Bragg reflector resonators reach approximately 130 in the 5–25 V range, after de-embedding of 1Ω series resistance.

Wideband measurements allow some evaluation on whether the Bragg reflector is correctly designed and fabricated. In Fig. 3.12 the measured real part of the resonator impedance is plotted along the calculated reflectivity response of the HfO_2/SiO_2 reflector stack. Good agreement between the peaks in the measured response and the minima of the calculated reflectivity indicate that the reflection band of the acoustic mirror is positioned correctly.

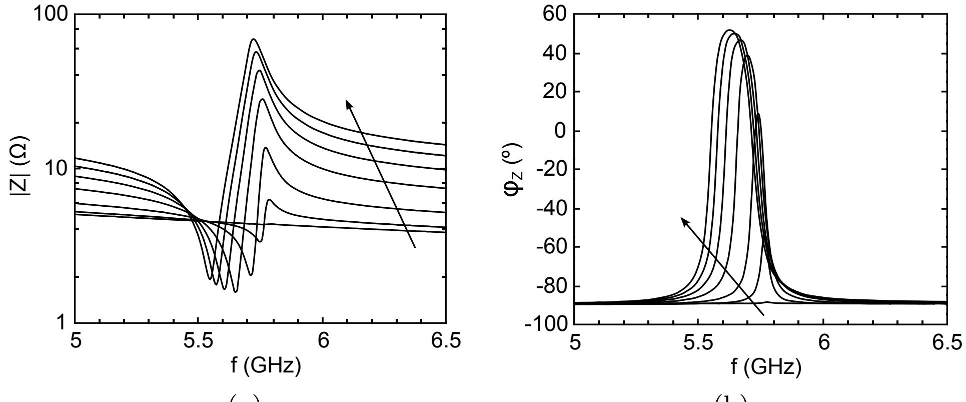

(a) (b)

Fig. 3.10: Measured magnitude (a) and phase (b) of a $Ba_{0.25}Sr_{0.75}TiO_3$ resonator input impedance. Arrows indicate increasing dc bias voltage 0, 2, 5, 10, 15, 20, and 25 V. HfO_2/SiO_2 Bragg reflector and Pt bottom electrode.

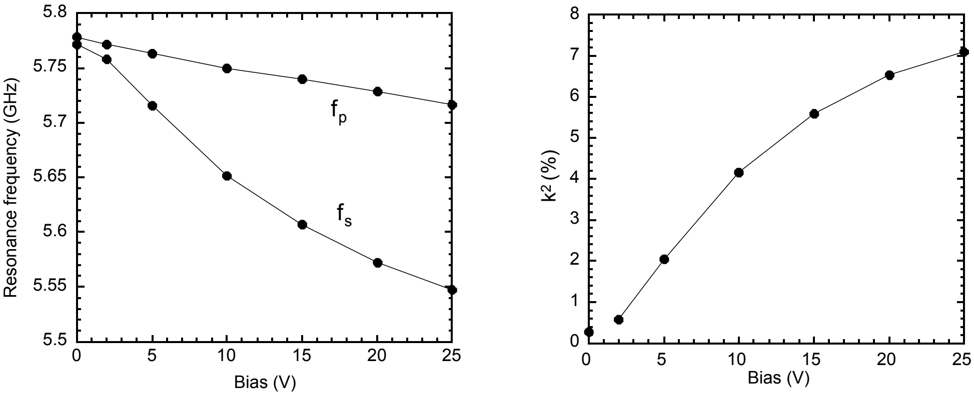

(a) (b)

Fig. 3.11: Series and parallel resonances (a) and effective coupling coefficient (b) as a function of dc bias voltage for $Ba_{0.25}Sr_{0.75}TiO_3$ resonator. HfO_2/SiO_2 Bragg reflector and Pt bottom electrode.

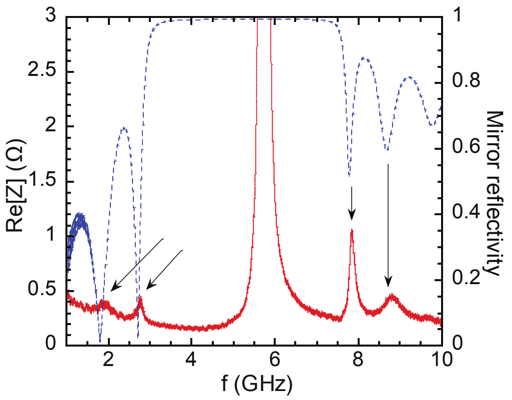

Fig. 3.12: Measured real part of resonator input impedance at 25 V dc bias (solid line) and calculated acoustic mirror reflectivity (dotted line) as a function of frequency. Arrows mark peaks associated with leakage of acoustic energy through the reflector.

3.4 Modeling and theory of induced piezoeffect

Modeling of the BSTO TFBAR characteristics is presented in Paper [D]. This modeling is based on solving the basic 1D equations for a thickness mode piezoelectric plate resonator taking into account mechanical loading [47]. The electrical input impedance of such a resonator is given by

$$Z = \frac{1}{j\omega C}\left[1 - k_t^2 \frac{\tan\phi}{\phi} Z_L\right], \tag{3.5}$$

where C is the capacitance of the parallel plate structure, k_t^2 is the electromechanical coupling coefficient of the active piezoelectric layer, and ϕ is the acoustic phase over the active layer. Z_L describes the effects of mechanical loading and is given by

$$Z_L = \frac{(z_t + z_b)\cos^2\phi + j\sin 2\phi}{(z_t + z_b)\cos 2\phi + j(z_t z_b + 1)\sin 2\phi}. \tag{3.6}$$

z_t and z_b are the acoustic impedances loading the resonator at the top and bottom interfaces, respectively, normalized to the impedance of the active layer. The load impedances for a multilayer structure can be computed by repeated use of the transmission line impedance equation (3.1).

Using the above equations a complete TFBAR structure can be simulated, assuming that all material properties are known. The observed dc field dependence of the tunable resonator frequency response is a result of the field dependent properties of the BSTO film, entering the above equations as field dependent permittivity, piezoelectric coefficient, coupling coefficient, etc. Theoretical models for this field dependence are obtained as a result of free energy expansions taking into account higher order dielectric and mechanical coupling terms [48, 49]. A qualitative

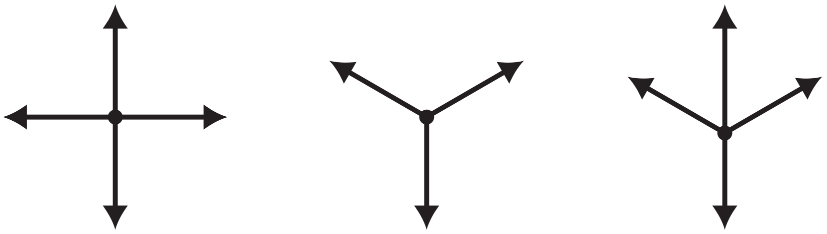

Fig. 3.13: Schematic representation of dipoles in centrosymmetric material (left), piezoelectric material (center), and originally centrosymmetric material under vertical dc field (right).

understanding of the appearance of a piezoeffect in paraelectric BSTO under dc bias can be obtained by considering the electrostrictive effect. In section 1.2 electrostriction, normally not included in the standard piezoelectric equations, was described as a field induced mechanical deformation or strain, S, quadratic in the polarization, P:

$$S = QP^2, \tag{3.7}$$

where Q is the electrostrictive coefficient. Writing the polarization as $P = P_{dc} + P_{ac}$ results in

$$S = Q(P_{dc} + P_{ac})^2 = QP_{dc}^2 + 2QP_{dc}P_{ac} + QP_{ac}^2. \tag{3.8}$$

The factor $2QP_{dc}$ can here be identified as an effective dc field dependent piezoelectric coefficient as seen by a low amplitude ac field, i.e. the material reveals a strain response linear with the low amplitude ac field if biased with a larger dc field. In principle the induced piezoeffect exists in all materials under dc bias, but is very weak except for certain materials such as ferroelectrics due to their high permittivity giving rise to a large polarization for a given electric field. An attempt to graphically illustrate the induced piezoeffect is made in Fig. 3.13, where the qualitative similarity of the piezoelectric material and the distorted originally centrosymmetric material under bias field is shown. Observe that for these two cases an applied small signal electric field or mechanical input results in mechanical and polarization responses, respectively, which change with the sign of the input, i.e. a piezoelectric effect.

Formal derivations of the field induced piezoeffect in paraelectric phase BSTO aimed at explaining the resonance behavior in BSTO TFBARs have been developed using either polarization [48] or displacement field [49] free energy expansions. Choosing mechanical strain and polarization as the independent variables leads to the following set of equations [48]:

$$k_t^2 = \frac{h^2 \chi_f^2}{c^D \epsilon}, \tag{3.9}$$

$$c^D = c^0 - m P_{dc}^2 - \frac{h^2 \epsilon_b}{1 + \epsilon_b / \chi_f}, \tag{3.10}$$

$$\epsilon = \epsilon_b + \chi_f, \tag{3.11}$$

$$h = h^0 + 2 q P_{dc}, \tag{3.12}$$

where h is the effective piezoelectric coefficient, χ_f is the field dependent ferroelectric contribution to the susceptibility, c^D is the elastic coefficient, ϵ is the permittivity, ϵ_b is the background permittivity, P_{dc} is the dc component of the polarization, q is the electrostriction coefficient, and m is a higher order electrostriction coefficient.

Modeling of the measured results in Fig. 3.8, based on (3.9)–(3.12) and (3.1), (3.5)–(3.6), was presented in Paper [D]. This modeling includes the acoustic effects of all layers in the resonator stack as well as the dc field dependence, see Fig. 3.14. Mechanical losses were introduced through complex propagation constants. The agreement between modeled and experimental results is in general good for bias voltages up to 10 V. The tunable TFBAR modeling presented here assumes purely longitudinal acoustic waves and perfectly smooth interfaces between all layers in the resonator stack. Under these conditions it is possible to reproduce the experimentally obtained TFBAR Q-factor by assuming an unexpectedly low mechanical Q-factor of the ferroelectric film. In a real device a number of additional loss mechanisms, not included in typical one-dimensional modeling, may contribute significantly to the total loss level of the resonator. Some of these loss mechanisms are discussed in section 3.6.1.

An equivalent circuit formulation based on the same piezoelectric relations as discussed above is referred to as the Mason model [50]. The Mason model is a three-port representation, see Fig. 3.15a, consisting of one electrical port representing the resonator electrodes, and two mechanical ports where mechanical loads to the upper and lower parts of the active layer are connected. This type of 1D resonator modeling, either based on direct use of the piezoelectric equations as in Paper [D], or equivalently, implemented in a circuit simulator (Mason model), takes materials properties and dimensions as inputs. This makes it a useful tool for quickly evaluating the effect of changes to the design of the resonator stack. Another commonly encountered model is the modified Butterworth-Van Dyke (MBVD) model [51], see Fig. 3.15b, consisting of six lumped elements. C_m, L_m and R_m model the acoustic properties of the active layer, while C_0 and R_0 represent the parallel plate capacitance and dielectric losses, respectively. Ohmic losses in electrodes are

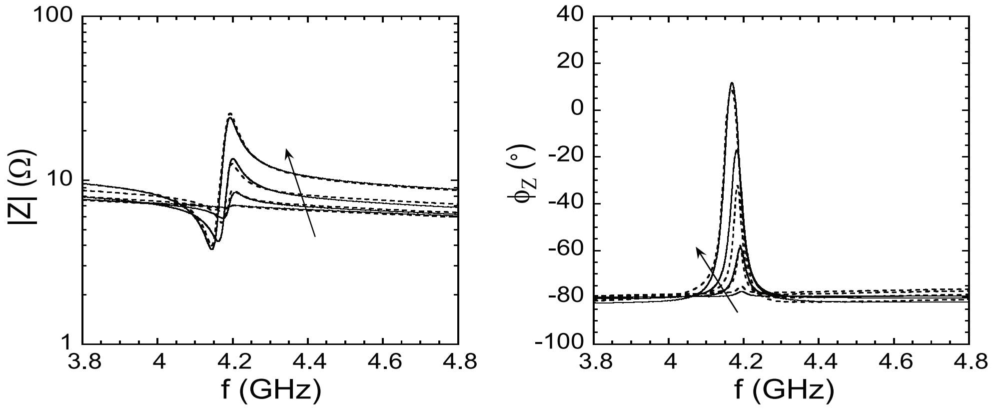

(a) (b)

Fig. 3.14: Magnitude (a) and phase (b) of the modeled (solid lines) and measured (dotted lines) $Ba_{0.25}Sr_{0.75}TiO_3$ TFBAR input impedance. Arrows indicate increasing bias voltage 0, 2, 5, 10 V.

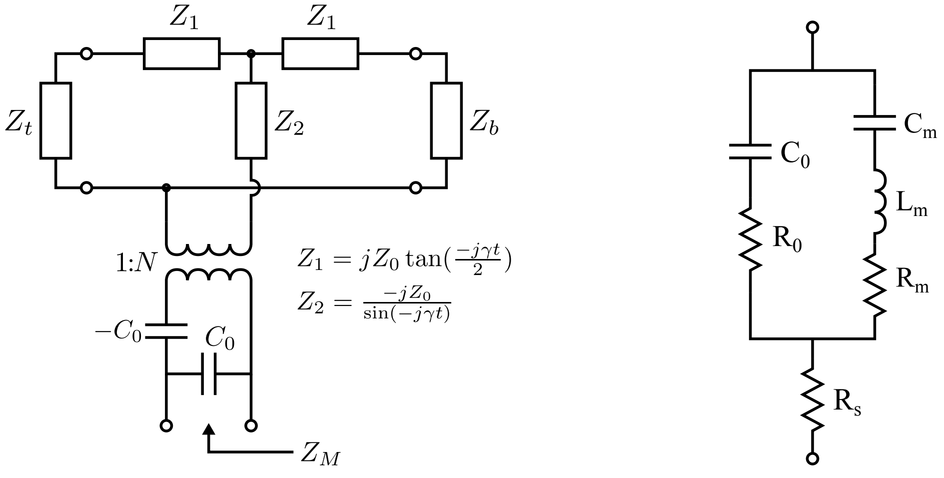

(a) (b)

Fig. 3.15: Mason model three-port representation of TFBAR (a), and lumped element MBVD model (b).

represented by R_s. The MBVD model of the TFBAR can be extracted from measurements and used to represent the resonator in circuit simulations [40, 52]. It is also widely used as a robust method for extracting the resonator Q-factor from measurements.

3.5 Temperature dependence studies

In section 3.3 (and in Paper [E]) it was shown that the characteristics of TFBARs based on $\mathrm{Ba_{0.25}Sr_{0.75}TiO_3}$ and $\mathrm{BaTiO_3}$ are different in terms of resonance frequency tuning direction. The difference in Curie temperature between the two active materials was assumed to be the reason and it motivated temperature dependence studies, presented in Paper [D]. The resonators are based on a Au/$\mathrm{SiO_2}$ Bragg reflector and Au bottom electrodes. A vacuum chamber/probe station equipped with a closed-cycle cryocooler was used for measurements at room temperature and down to cryogenic temperatures, and a hot chuck was used for heating. Resonance frequencies as a function of temperature are shown in Fig. 3.16 for a $\mathrm{Ba_{0.25}Sr_{0.75}TiO_3}$ resonator, measured in the range 40–420K, and for a $\mathrm{BaTiO_3}$ resonator, measured from room temperature up to 520K.

Considering first the low bias measurements it can be observed that the series and parallel resonance frequencies of the $\mathrm{Ba_{0.25}Sr_{0.75}TiO_3}$ sample reveal a step at approximately 150K, followed by a decrease with temperature. (The discontinuity at 300K is due to the transfer of the sample from the cryobox to the setup used for heating.) The $\mathrm{BaTiO_3}$ resonance frequencies on the other hand increase with temperature in the whole measured range. These general changes can be explained by the intrinsic temperature dependence of corresponding bulk material properties. In the ideal case with perfect boundary conditions, $Z_L = 1$ in (3.5), f_p and f_s can be written as [53]

$$f_p = \frac{v_a}{2t} \tag{3.13}$$

and

$$f_s = \frac{v_a}{2\pi t}\sqrt{\pi^2 - 8k_t^2}, \tag{3.14}$$

i.e. they are proportional to the acoustic velocity, $v_a = \sqrt{c^D/\rho}$, of the resonator active layer. Bulk single crystal data for $\mathrm{SrTiO_3}$ reveal a step in the acoustic velocity and elastic coefficient at the phase transition at 105K, after which they gradually decrease with increasing temperature [2], qualitatively explaining the $\mathrm{Ba_{0.25}Sr_{0.75}TiO_3}$ resonances above. $\mathrm{BaTiO_3}$ single crystals also reveal a step in the elastic constant at the phase transition temperature around 120°C, after which it increases with temperature [2]. This may explain the $\mathrm{BaTiO_3}$ resonances above if the phase transition temperature in the film is assumed to be

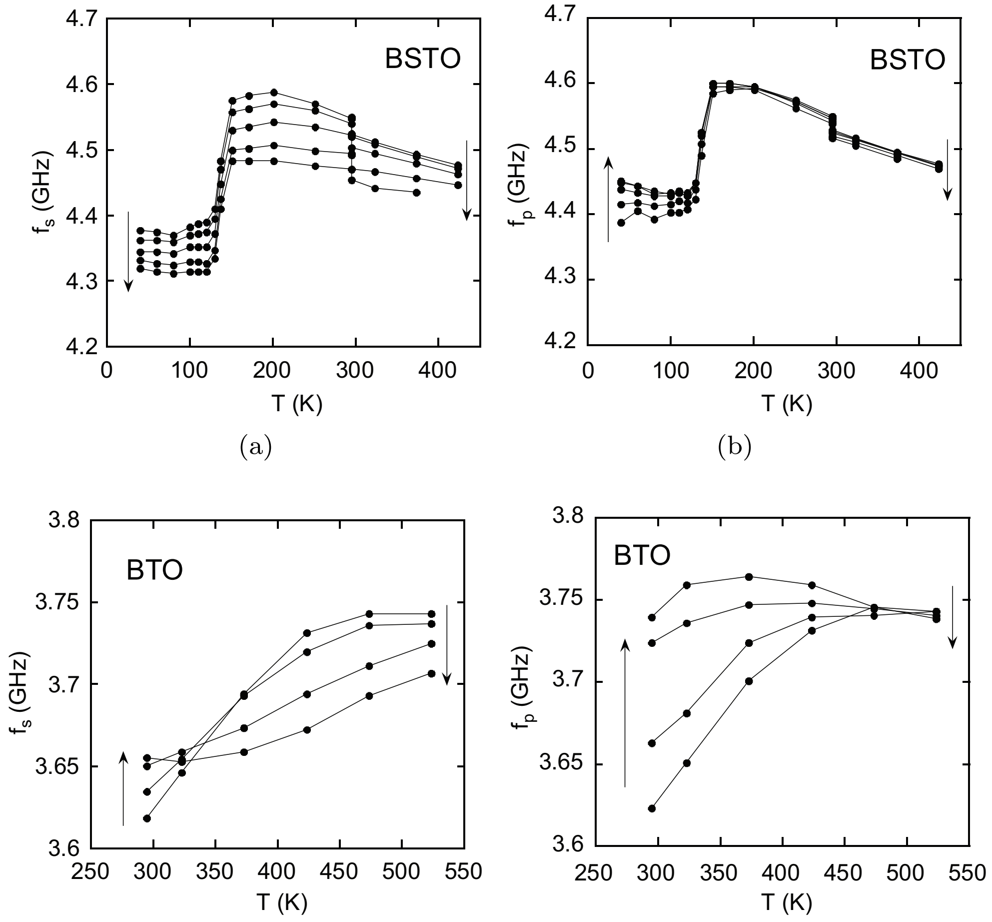

(a) (b)

(c) (d)

Fig. 3.16: Resonance frequencies as a function of temperature for $Ba_{0.25}Sr_{0.75}TiO_3$ resonator (a,b) and $BaTiO_3$ resonator (c,d). Arrows indicate increasing bias voltage 0, 2, 5, 10, 15 V for the $Ba_{0.25}Sr_{0.75}TiO_3$ resonator and 2, 5, 10, 15 V for the $BaTiO_3$ resonator.

shifted close to room temperature. Low frequency measurements of the film permittivity, see Fig. 3.17, support this shift since the permittivity maximum for the $BaTiO_3$ film appears close to room temperature.

The different tuning characteristics observed for the two compositions are more difficult to explain fully. Considering e.g. the parallel resonance, a qualitative similarity between the $Ba_{0.25}Sr_{0.75}TiO_3$ and $BaTiO_3$ resonators can be seen in that they both tune towards higher frequencies at low temperatures, and towards lower frequencies at high temperatures. The tuning direction switch in the $Ba_{0.25}Sr_{0.75}TiO_3$ case roughly corresponds to the position of the presumed phase transition, while the switch for $BaTiO_3$ occurs at a temperature much higher than room temperature. Using (3.10) and (3.13) this effect may in principle be explained by a change in the sign of the parameter m, which to a

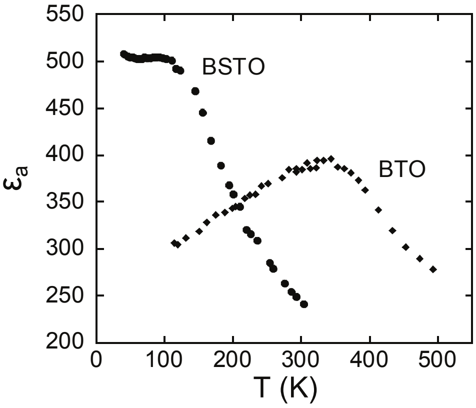

Fig. 3.17: Apparent permittivity as a function of temperature for the $Ba_{0.25}Sr_{0.75}TiO_3$ and $BaTiO_3$ films, extracted from 1 MHz capacitance measurements.

large extent determines the tuning characteristics of the elastic coefficient and thus the acoustic velocity and parallel resonance frequency. Measurements of single crystal $SrTiO_3$ reported in the literature [2] however show that the elastic coefficient is decreasing with bias field both below and above the phase transition. Further studies aimed at a more complete understanding of the temperature dependent properties may help in selecting the optimal $Ba_xSr_{1-x}TiO_3$ composition in order to maximize resonator tunability, coupling coefficient and Q-factor.

3.6 Resonator performance

Whether or not a resonator is suitable for use in a specific practical circuit is mainly determined by the performance in terms of coupling coefficient and Q-factor. The bandwidth of a typical ladder type band pass filter based on series and shunt resonators is primarily limited by the effective coupling coefficient of the resonators [41]. The passband insertion loss and steepness of the filter skirts on the other hand depend on the Q-factor [54]. In an oscillator application only one of the resonances is used, and the Q-factor is of main importance since the oscillator phase noise is closely linked to the resonator phase slope [55].

Compared to fixed frequency AlN based resonators the effective resonator coupling coefficient achieved in this work is comparable or slightly higher, at high bias, see Fig. 3.11b. The presented Q-factor of the tunable resonators are however low in comparison. Whether this is due to intrinsic properties of BSTO, or extrinsic fabrication or design issues, is considered in the following section.

3.6.1 Q-factor reduction mechanisms

The general definition of a resonator Q-factor involves the ratio between stored energy and dissipated energy per cycle. Identifying possible resonator energy leakage paths and loss mechanisms is thus crucial in order to increase the TFBAR Q-factor. Explaining the relatively low Q-factor of the TFBARs presented in this work is however not straight forward, and several possible limitations exist whose impact are largely unknown and difficult to estimate without specific studies.

- The intrinsic mechanical Q-factor of the BSTO material, as determined by its viscoelastic behaviour [53, 26], can be estimated by extrapolation from lower frequency measurements. This results in a mechanical Q-factor for $SrTiO_3$ of approximately 1200 at 5 GHz [46], indicating that fundamental viscoelastic losses are not dominant in the resonators presented in this thesis.

- Dielectric losses in the ferroelectric film can be taken into account in the TFBAR simulation (section 3.4) in analogy with varactor modeling [7], as a conductance in parallel to the impedance calculated using Eq. (3.5). It is observed that high dielectric losses mainly impact on the Q-factor at the parallel resonance frequency. Measured dielectric loss tangents are however considerably lower than what would be required to reduce the resonator Q-factor considerably.

- Ohmic losses in lead strips, contacts, and electrode plates generally impact mainly on the Q-factor at the series resonance frequency, where the resonator impedance is very low and currents are high [56]. The Q-factor at the parallel resonance frequency, where the impedance is high, on the other hand is only marginally affected by an additional resistivity contribution. Series resistance of the lead strips and contacts have been de-embedded in a straight-forward way for the resonators presented in this work, without affecting extracted the Q-factor considerably.

- Acoustic leakage has been quite extensively considered for AlN based resonators, especially for the solidly mounted design, where an acoustic leakage path into the substrate exists through the reflector structure. Mirror layers deviating from the $\lambda/4$ thickness will result in energy losses for each reflection. In addition, it has been shown that generation of shear waves, which are not effectively reflected by the mirror designed for longitudinal mode due to lower acoustic velocity, can reduce the resonator Q-factor considerably [54]. Confinement of these shear waves can be improved by a compromising optimization of the reflector layers (deviating

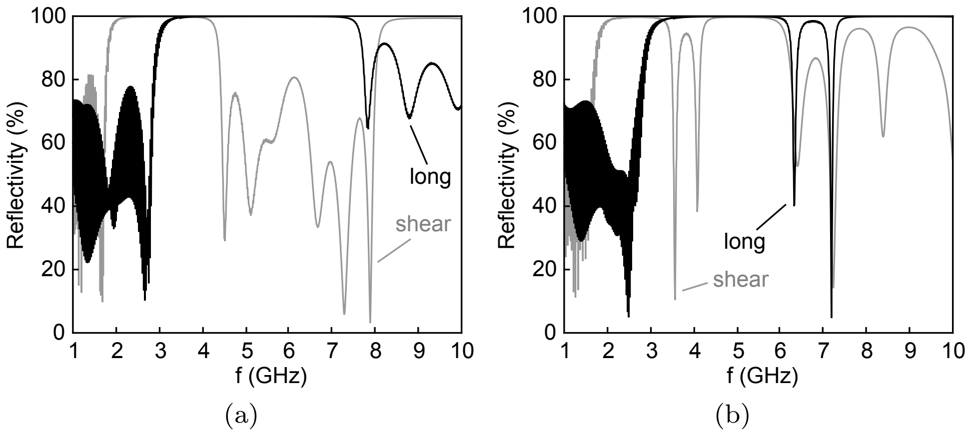

Fig. 3.18: Calculated reflectivity of (a) longitudinal $\lambda/4$ Bragg reflector, and (b) reflector designed to reflect both longitudinal and shear waves at 5.25 GHz.

from the longitudinal $\lambda/4$ condition) to support reflection of both longitudinal and shear waves [54]. Fig. 3.18 shows calculated reflectivities for longitudinal and shear waves for two versions of HfO_2/SiO_2 reflectors. It can be clearly seen that shear waves to a large extent leak through the reflector stack with the conventional design, Fig. 3.18a, while the co-optimized version reflects both longitudinal and shear waves at the design frequency, Fig. 3.18b.

- Surface and interface roughness may be detrimental to resonator Q-factor due to scattering of acoustic waves and possibly resonance broadening effects. It has been reported that the Q-factor of AlN based TFBARs is not currently limited by the effects of surface and interface roughness [57, 26]. From the perspective of tunable BSTO TFBARs two observations can be made with respect to this claim: i) The frequency considered (~2 GHz) is lower than what has been the focus of most tunable TFBAR studies (~5 GHz). ii) The acoustic velocity of AlN (~11000 m/s) is higher than for BSTO (~6000 m/s). These differences combined result in a considerably higher roughness to wavelength ratio in the BSTO resonator case, and possibly much more pronounced Q-factor reduction even at moderate roughness levels of only a few nm. In Paper [A] attempts are made to estimate the effect of thin film roughness using two models: i) Acoustic wave attenuation due to roughness induced diffuse scattering, and ii) treating the BSTO active layer as an assembly of a large number of individual resonators acting in parallel.

- Effects due to the finite lateral size of the resonators, such as generation of lateral modes or perimeter leakage effects due to non-vertical components of the acoustic waves may limit the resonator Q-factor. Due to the relatively small size of the tunable TFBARs presented in this thesis (due to the high capacitance density) these effects may be more pronounced than for the conventional AlN based TFBARs.

As shown above there are several mechanisms which may limit the Q-factor of the tunable TFBAR, perhaps in a slightly different manner and extent than for the well developed AlN resonators. Further studies are needed in order to increase the understanding of these mechanisms and whether they can be overcome by more careful design or fabrication optimizations.

3.7 Conclusions

During the course of this work a few research groups have presented results on $Ba_xSr_{1-x}TiO_3$ TFBARs, summarized in Table 3.1. Reflector based as well as membrane type resonators have been reported, in the frequency range 1.6–7 GHz. Three out of six research groups (including Chalmers) have chosen to work on a reflector based approach, while the three other groups focus on a membrane design.

At Chalmers two different routes have been explored. The first route, the results of which are presented in this thesis, focuses on BSTO films grown by PLD and a resonator design based on a non-conducting Bragg reflector stack for improved integration possibilities. The other route involves BSTO films grown by magnetron sputtering, on primarily W/SiO_2 Bragg reflector stacks [46, 58, 59]. Some differences can be observed when comparing the results of these two routes, see Table 3.1. The Q-factor of the magnetron sputtered resonators based on W/SiO_2 reflectors are considerably higher than for the corresponding resonators presented in this work, ~350 [46] compared to ~130 [Paper [B]]. The maximum allowed dc field before device breakdown is also higher, ~172 V/µm [59], compared to ~107 V/µm [Paper [B]]. Despite the advantage in breakdown field, the measured effective coupling coefficient (and resonance tunability) for the sputtered samples is lower, ~4.4% (~2%) [59] compared to ~7.1% (3.8%) [Paper [B]]. If the comparison is made at the same bias field the difference is even more pronounced. Effects of interface roughness has been identified as one possible explanation to the difference in resonator Q-factor. In Ref. [58] TFBARs based on magnetron sputtered BSTO films on two different Bragg reflectors, W/SiO_2 and HfO_2/SiO_2, were studied. In this study a higher Q-factor of the TFBAR based on the W/SiO_2 reflector was explained by a less pronounced surface roughness. The work presented in Ref. [59] also suggests that roughness may be a critical issue.

From Table 3.1 it can be seen that the reported results from Chalmers are leading in terms of Q-factor [46] and coupling coefficient and tunability [Paper [B]]. Apart from comparisons of the actual performance parameters, analysis of differences and trends in the various published results is however difficult. The data spread is large, indicating that individual fabrication conditions are highly influential on the final results. Factors such as active layer thickness, resonance frequency, electrode configuration, maximum bias field, etc. are also quite different between the published results, making direct comparisons problematic. In addition possibly crucial properties such as film roughness are seldom reported.

Table 3.1: Compilation of $Ba_xSr_{1-x}TiO_3$ TFBAR publications.

Ref.	Material	f_{res} (GHz)	Q	Tunability f_s (f_p) (%)	k^2 (%)	Max field (V/µm)	BST thickness (nm)	Type	Bottom el.	Top el.
Paper [B] (2011)	BST 25/75	5.7	130	3.8 (0.9)	7.1	107	234	Reflector, HfO_2/SiO_2	Pt, 100nm	Al, 100nm
Paper [D] (2008)	BST 25/75	4.2	120	1.7 (0.3)	3.7	43	350	Reflector, Au/SiO_2	Au, 80nm	Al/Au, 110/20nm
Paper [E] (2007)	BST 25/75	4.4	120	1.6 (1.3)	0.5	40	350	Reflector, Au/SiO_2	Au, 80nm	Al, 140nm
Paper [E] (2007)	$BaTiO_3$	3.8	30	1.3 (4)	6.2	30	350	Reflector, Au/SiO_2	Au, 80nm	Al, 140nm
[46] (2010)	BST 25/75	5.1	350	1	2.3	86	290	Reflector, W/SiO_2	Pt, 100nm	Al, 100nm
[59] (2011)	BST 25/75	5.4	250	2	4.4	172	290	Reflector, W/SiO_2	Pt, 100nm	Al, 100nm
[60] (2007)	$SrTiO_3$	5.8	78	1	2	125	60	Reflector, Pt/SiO_2	Pt	Pt
[61] (2008)	$SrTiO_3$	7	100	1	3.3	150	60	Reflector, Pt/SiO_2	Pt	Pt
[62] (2008)	$SrTiO_3$	2.2	50	1.6 (0.6)		70	430	Reflector, W/SiO_2	Pt, 140nm	Pt/Au, 80/100nm
[63] (2007)	BST 30/70	6.7		1.2 (0.4)	2	67	300	Membrane	Pt, 100nm	Al, 300nm
[48] (2007)	BST 30/70	2.9		2 (0.5)	3.6	73	550	Membrane	Pt, 100nm	Al, 300nm
[64] (2008)	BST 30/70	2.8	200	2.4 (0.6)	4.4	62	650	Membrane	Pt, 100nm	Al, 300nm
[65] (2007)	BST	2	220		7	34	730	Membrane	Pt, 100nm	Pt, 100nm
[66] (2008)	BST 70/30	1.6	20		20 (?)	71	1050	Membrane	Pt, 80nm	Pt, 80nm
[66] (2008)	BST 70/30	1.6	<50		12 (?)	69	580	Membrane	Pt, 200nm	Pt, 200nm

Chapter 4

Switchable filter

Filtering applications have been the driving force for the AlN based TFBAR technology, and several filter topologies have been realized. Electrically coupled ladder and lattice filters, as well as acoustically coupled filters of different types have been demonstrated [26]. Recently dc field switchable TFBAR filters based on polar phase [67] and paraelectric phase [68, 69] ferroelectrics have also been considered. During this work ladder type bandpass filters based on BSTO TFBARs have been designed and fabricated.

4.1 Filter design and simulation

Fig. 4.1a shows a schematic of a ladder filter consisting of two series resonators (RS1, RS2) and one parallel resonator (RP). In line with the general ladder filter design the series resonance frequencies of RS1 and RS2 are chosen to approximately coincide with the parallel resonance frequency of RP. At this frequency the signal passes through the filter by means of the low impedance path presented by RS1 and RS2 (at series resonance), while leakage to ground is blocked by the high impedance RP (at parallel resonance), resulting in a low insertion loss passband. The filter design and simulation is based on measurements of the BSTO based TFBARs presented in Paper [B]. The filter layout, see Fig. 4.2a, is designed for measurements with ground-signal-ground microprobes, and allows bias to be applied to the three resonators individually.

Simulated filter characteristics (co-simulation, ADS Momentum + BVD circuit) for the ’on’ (25V bias) and ’off’ (no bias) states, see Fig. 4.2, clearly show the switching behavior of the filter. The ’on’ state reveals an insertion loss of 2.9 dB, and a 3 dB bandwidth of 176 MHz (3.1%). These characteristics can be compared to the data for a commercially available AlN based filter from TriQuint, designed for WLAN applications at 5.775 GHz (TriQuint 880369). The specified typical 3 dB bandwith of this filter is 145 MHz (2.5%), and the insertion loss 3 dB.

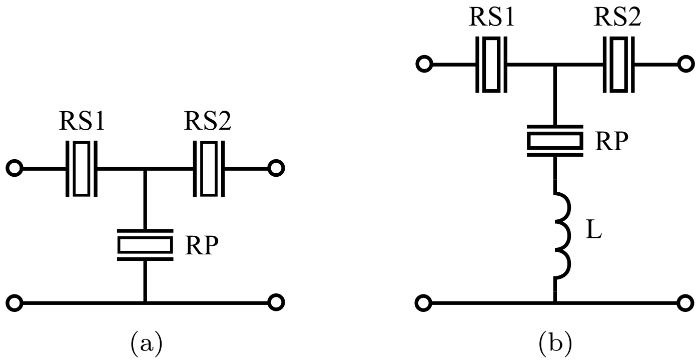

Fig. 4.1: Schematics of two versions of BSTO TFBAR ladder filters.

Based on this comparison the simulated performance of the switchable filter looks very promising. The main difference is the level of out of band rejection, which for the TriQuint filter is more than 20 dB, compared to only 10 dB for the simulated switchable filter.

Out of band rejection can be improved by adding more sections to the ladder circuit, at the cost of a higher in-band insertion loss. An alternative approach is schematically shown in Fig. 4.1b where an inductor has been added between the parallel resonator and the ground [26]. In the passband RP is close to parallel resonance and the inductor barely affects the circuit. The out of band response can however be improved if the inductor is chosen to series resonate with RP close to the filter center frequency. Outside the passband, where RP is capacitive, this series resonance results in an improved rejection. Fig. 4.3 shows one version of a filter layout where an inductive section has been added, including simulated performance. As can be seen the out of band characteristics is considerably improved. The 'off' state rejection is also improved as a result of the LC resonance. Due to the difference in capacitance of RP in the 'on' (low permittivity) and 'off' (high permittivity) states, the value of the inductance needs to be carefully chosen in order to maximize both extinction ratio and out of band rejection.

4.2 Fabrication and measurements

Fabrication of filter structures was performed using high resistivity Si wafers covered with HfO_2/SiO_2 Bragg reflector layers. TiO_2/Pt bottom electrodes were deposited by magnetron sputtering and patterned using Ar ion milling. The $Ba_{0.25}Sr_{0.75}TiO_3$ active layers were deposited by PLD. Al top electrodes were deposited by magnetron sputtering and patterned using a lift-off process. Two different lithography masks for the top electrodes enabled proper shifting of the parallel resonator resonance by deposition of a slightly thicker electrode. A thick Au electrode was evaporated and patterned using lift-off.

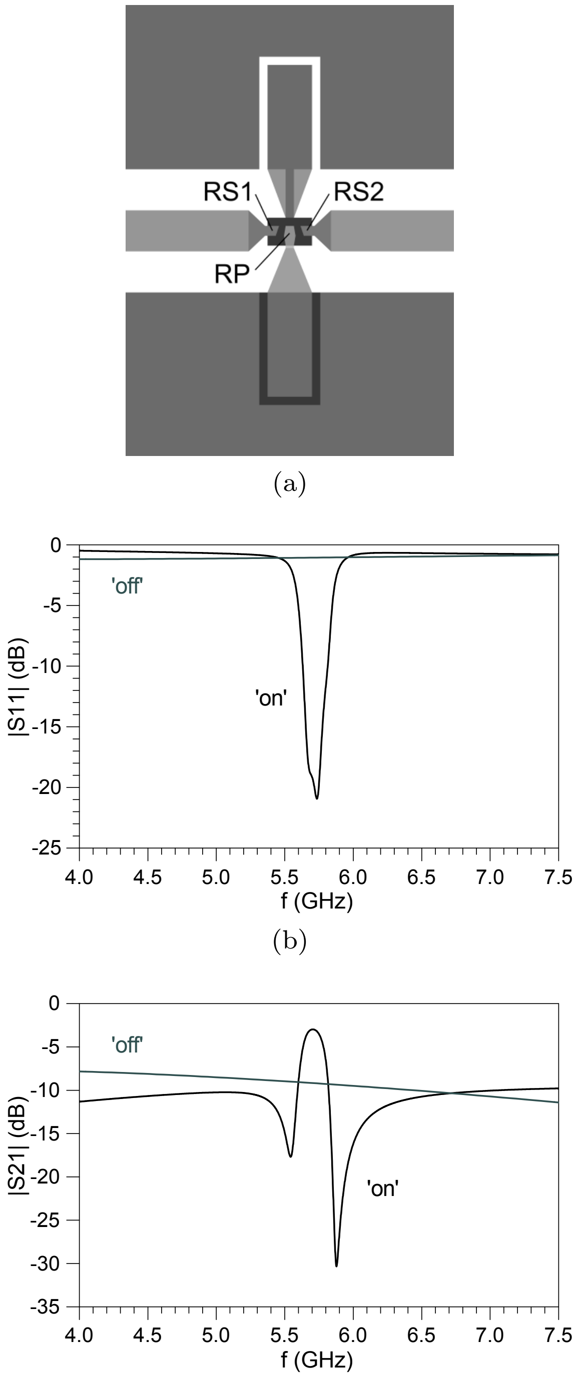

(a)

(b)

(c)

Fig. 4.2: Filter layout (a) and simulated characteristics (b, c). Version without added inductance, corresponding to the schematic in Fig. 4.1a

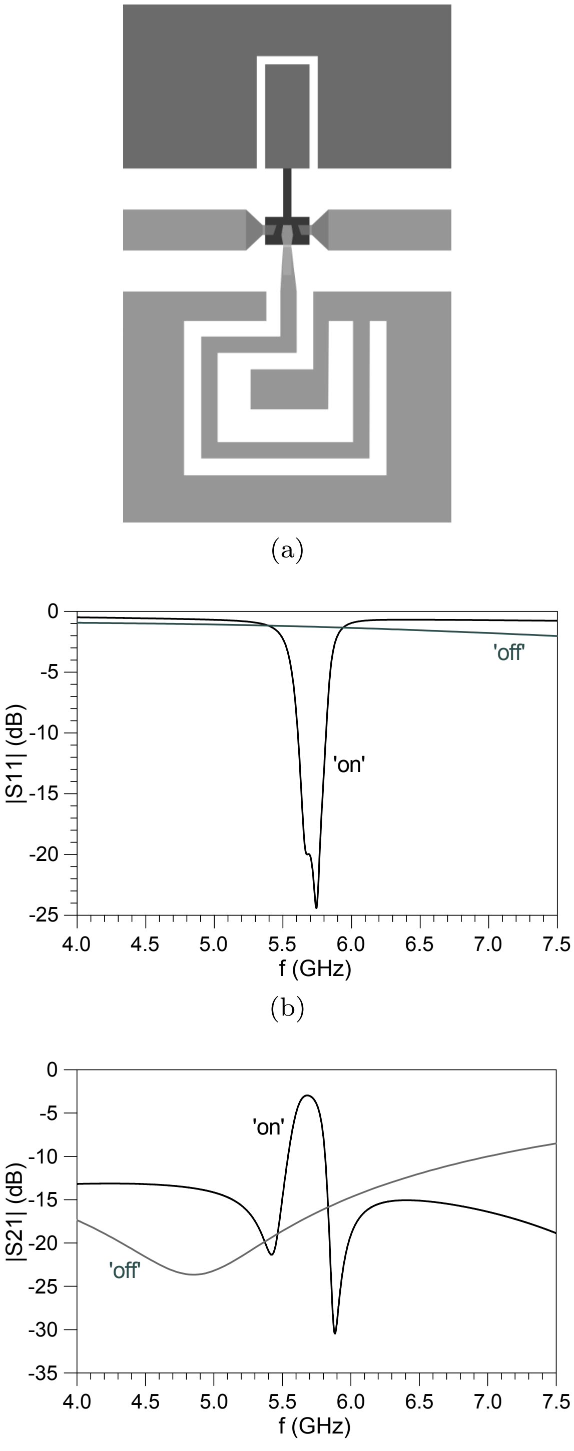

(a)

(b)

(c)

Fig. 4.3: Filter layout (a) and simulated characteristics (b,c). Version with added inductance, corresponding to the schematic in Fig. 4.1b

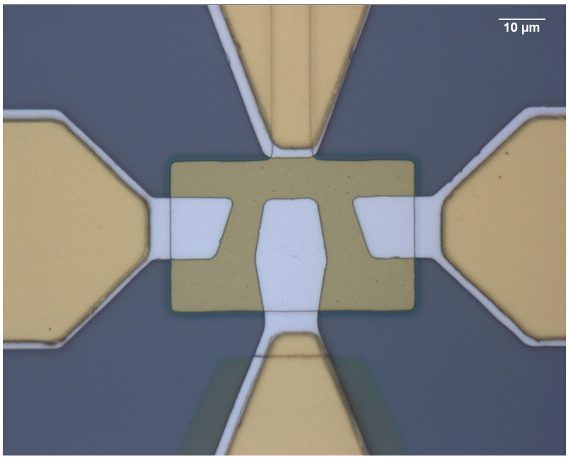

Fig. 4.4: Optical image of fabricated filter (central section).

The more complex fabrication process turned out to put more stringent requirements on the bottom electrode than the previous processing of simple circular structures on non-patterned bottom electrodes. Adhesion problems were encountered, frequently delaminating filter structures completely from the substrate. Cross section SEM images identified the TiO_2/Pt interface as the delamination interface. Reducing the PLD growth temperature to 620° made it possible to successfully fabricate and measure a few filter structures of the type without the additional inductor, see Fig. 4.4 for an image of the fabricated filter. The individual resonator Q-factor on this substrate is however, mainly due to the non-optimal growth temperature, considerably lower than what was presented in Paper [B] and used for the filter design and simulations. This results in measured filter characteristics which does not reproduce the simulated results, see Fig. 4.5. Compared to the previously reported BSTO TFBAR filter in Ref. [68] the results of Fig. 4.5 present a higher insertion loss of 5.95 dB (4.26 dB [68]), partly explainable by the additional series resonator compared with the L-section design used in Ref.[68].

In conclusion it can be noted that the measured filter characteristics are somewhat disappointing compared with the promising simulated results. The concept of a switchable bandpass filter is however clearly demonstrated. The reason for the poor performance is known (low Q-factor of resonators due to bottom electrode issues), and adjustments of the fabrication process are expected to improve the measured filter performance considerably.

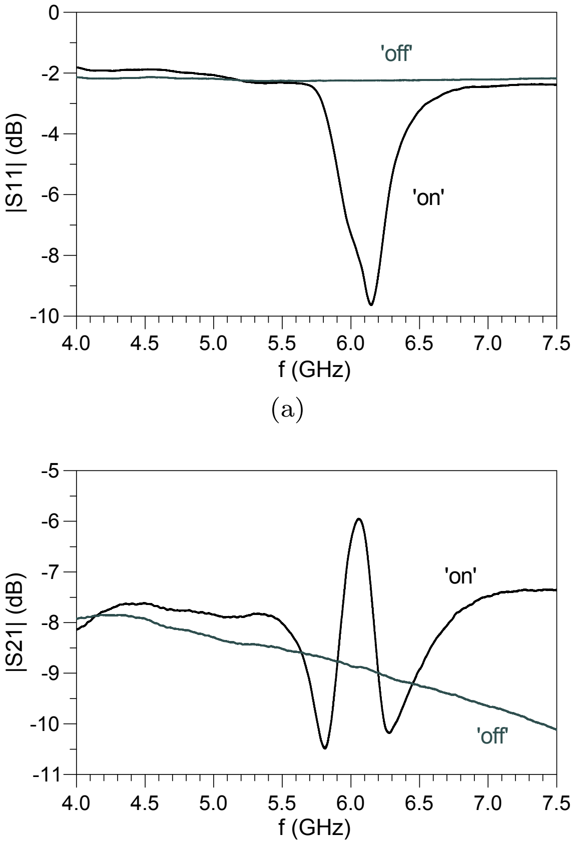

(a)

(b)

Fig. 4.5: Measured characteristics of fabricated filter. The 'off' state is obtained at zero bias. In the 'on' state the resonators are biased at 15V (RS1), 15V (RS2), and 25V (RP).

Chapter 5

Summary and outlook

The main achievement of this work has been the demonstration, characterization, and development of a novel type of electrically switchable and tunable thin film bulk acoustic wave resonator. The resonators are based on primarily paraelectric phase $Ba_{0.25}Sr_{0.75}TiO_3$ thin films and reveal a non-hysteretic tuning response as a result of the pronounced electric field induced piezoelectric effect.

In terms of resonator performance the achieved effective electromechanical coupling coefficient at high dc bias, 7.1%, is comparable to corresponding AlN based fixed frequency resonators. The series resonance frequency tunability reaches 3.8%, corresponding to an absolute tunability of approximately 200 MHz, the highest reported for non-hysteretic tunable TFBARs. The Q-factor however is considerably lower than what could be expected based on comparisons with fixed-frequency counterparts. It should however be pointed out that the BSTO TFBARs should primarily be compared to existing *tunable* technologies, such as resonators based on semiconductor or ferroelectric varactors. From this perspective the already obtained Q-factor of the TFBARs is not as poor as a direct comparison with the fixed frequency AlN counterpart would imply. The Q-factor of $\sim$130 achieved in this work is already competitive to e.g. varactor based LC resonators, due to the limited varactor Q-factor.

Further work should be focused on understanding more thoroughly which loss mechanisms are dominant and which countermeasures can be applied within resonator design and fabrication development. Studies indicate that interface roughness of the layers in the acoustic path is currently limiting the Q-factor of BSTO resonators based on HfO_2/SiO_2 resonators [58]. It needs to be determined if roughness generating effects, such as strain, in the HfO_2/SiO_2 reflector can be alleviated or if an alternative reflector design should be considered.

Studies aiming at understanding the observed differences in performance between resonators based on BSTO films grown by magnetron sputtering and PLD could give valuable information. Possibly then resonators with a combined high effective coupling coefficient and tunability (characteristic of PLD samples on HfO_2/SiO_2 reflector) and a high Q-factor (characteristic of sputtered samples on W/SiO_2 reflector [46]) could be achieved.

Preliminary results from a switchable bandpass filter based on the BSTO TFBARs have also been presented. The filter performance is limited by the very low Q-factor of the individual resonators on the measured filter substrate. This is a result of fabrication issues related to the bottom electrode adhesion, which turned out to be insufficient for the more complex filter fabrication process. Further efforts need to be put on the bottom electrode fabrication in order to obtain a more robust reflector/electrode interface. Although the demonstrated performance of the fabricated filter at this stage does not come close to the simulated results, the concept of a switchable filter is clearly demonstrated.

5.1 Summary of appended papers

Device fabrication was performed in the Nanofabrication laboratory at Chalmers. Material characterization and measurements were performed at Chalmers.

Paper A, Impact of thin film roughness on the performance of tunable bulk acoustic wave resonators

Two models are explored in order to estimate the impact of thin film roughness on the Q-factor of $Ba_{0.25}Sr_{0.75}TiO_3$ TFBARs. My contributions: Model development with co-authors, writing the paper.

Paper B, Tunable bulk acoustic wave resonators based on $Ba_{0.25}Sr_{0.75}TiO_3$ thin films and a HfO_2/SiO_2 Bragg reflector

A resonator design based on a non-conducting Bragg reflector stack and a Pt bottom electrode is presented. Considerably improved resonator effective coupling coefficient and tunability is achieved. My contributions: Development of Bragg reflector and bottom electrode fabrication, measurements, writing the paper.

Paper C, The effect of Bragg reflectors on the electromechanical performance of parallel-plate ferroelectric capacitors

Pronounced losses in parallel plate $Ba_xSr_{1-x}TiO_3$ varactors under dc bias are explained by electro-acoustic activity as a result of the field induced piezoelectric effect. My contributions: Fabrication, measurements, writing the paper.

Paper D, Field and temperature dependent parameters of the dc field induced resonances in $\mathbf{Ba}_x\mathbf{Sr}_{1-x}\mathbf{TiO}_3$-based tunable thin film bulk acoustic resonators

A resonator design suitable for circuit integration is introduced. Field and temperature dependence of $Ba_{0.25}Sr_{0.75}TiO_3$ and $BaTiO_3$ TFBARs are studied. Room temperature measurements are modeled using 1D transmission line equations and theory for field induced piezoelectric effect. My contributions: Development of fabrication process, SEM characterization, measurements, resonator modeling, writing the paper.

Paper E, Tunable solidly mounted thin film bulk acoustic resonators based on $\mathbf{Ba}_x\mathbf{Sr}_{1-x}\mathbf{TiO}_3$ films

Tunable bulk acoustic wave resonators based on $Ba_{0.25}Sr_{0.75}TiO_3$ and $BaTiO_3$ films are reported. My contributions: Development of fabrication process, SEM characterization, measurements, writing the paper.

Paper F, The effect of growth temperature on the nanostructure and dielectric response of $\mathbf{BaTiO}_3$ ferroelectric films

$BaTiO_3$ films grown by PLD at different substrate temperatures are studied using parallel-plate varactor structures. Correlations between growth temperature, film properties, and microwave performance are explored. My contributions: Fabrication, SEM and AFM characterization, measurements, model development with co-authors, writing the paper.

Acknowledgments

I would like to thank my supervisor Prof. Spartak Gevorgian for his support and guidance, always with enthusiasm and optimism, during my years in his group.

My supervisor Andrei Vorobiev for invaluable discussions and tutoring regarding experimental work.

Martin Norling for rewarding discussions related to TFBARs, ferroelectrics, and general microwave issues.

Tomas Liljenfors and Markus Löffler for help with electron microscopy studies.

Janusz Kanski for help with AES studies.

The staff of the Nanofabrication laboratory, especially Henrik Frederiksen for continuous support with thin film deposition systems and processes.

Past and present colleagues and friends at MEL/PEL/TML.

Thank you Maria ♥

This work was financially supported by the European Commission FP6 project NANOSTAR and the Swedish Research Council project VR-FBAR.

Bibliography

[1] R. E. Newnham, V. Sundar, R. Yimnirun, J. Su, and Q. M. Zhang, "Electrostriction: Nonlinear Electromechanical Coupling in Solid Dielectrics," *J. Phys. Chem. B*, vol. 101, no. 48, pp. 10 141–10 150, 1997.

[2] *Landolt-Börnstein, New Series*, vol. III/36A1, Springer-Verlag, 2001.

[3] R. Waser, Ed., *Nanoelectronics and Information Technology - Advanced Electronic Materials and Novel Devices.* Wiley-VCH, 2003.

[4] F. Jona and G. Shirane, *Ferroelectric Crystals.* Pergamon Press, 1962.

[5] A. K. Tagantsev, V. O. Sherman, K. F. Astafiev, J. Venkatesh, and N. Setter, "Ferroelectric materials for microwave tunable applications," *J. Electroceram.*, vol. 11, no. 1-2, pp. 5–66, 2003.

[6] G. H. Haertling, "Ferroelectric Ceramics: History and Technology," *J. Am. Ceram. Soc.*, vol. 82, no. 4, pp. 797–818, 1999.

[7] S. Gevorgian, A. Vorobiev, and A. Deleniv, *Ferroelectrics in Microwave Devices, Circuits and Systems.* Springer, 2009.

[8] J. F. Scott, *Ferroelectric Memories.* Springer, 2000.

[9] D. Damjanovic, "Ferroelectric sensors," *IEEE Sensors J.*, vol. 1, no. 3, pp. 191–206, 2001.

[10] P. Muralt, "Piezoelectrics in micro and nanosystems: Solutions for a wide range of applications," *J. Nanosci. Nanotechnol.*, vol. 8, no. 5, pp. 2560–2567, 2008.

[11] M. Ohring, *Materials science of thin films - Deposition and structure.* Academic press, 2002.

[12] G. W. Dietz, W. Antpohler, M. Klee, and R. Waser, "Electrode influence on the charge transport through SrTiO3 thin films," *J. Appl. Phys.*, vol. 78, no. 10, pp. 6113–21, 1995.

[13] T. Liljenfors, “The role of interfaces in oxide thin films,” Ph.D. dissertation, Chalmers University of Technology, 2007.

[14] A. Vorobiev, P. Rundqvist, K. Khamchane, and S. Gevorgian, “Silicon substrate integrated high Q-factor parallel-plate ferroelectric varactors for microwave/millimeterwave applications,” *Appl. Phys. Lett.*, vol. 83, no. 15, pp. 3144–3146, 2003.

[15] O. G. Vendik and S. P. Zubko, “Ferroelectric phase transition and maximum dielectric permittivity of displacement type ferroelectrics (BaxSr1-xTiO3),” *J. Appl. Phys.*, vol. 88, no. 9, pp. 5343–50, 2000.

[16] A. Vorobiev, P. Rundqvist, K. Khamchane, and S. Gevorgian, “Microwave loss mechanisms in Ba0.25Sr0.75TiO3 thin film varactors,” *J. Appl. Phys.*, vol. 96, no. 8, pp. 4642–4649, 2004.

[17] P. Bao, T. J. Jackson, X. Wang, and M. J. Lancaster, “Barium strontium titanate thin film varactors for room-temperature microwave device applications,” *J. Phys. D*, vol. 41, no. 6, p. 063001, 2008.

[18] H. C. Seong, L. B. Taek, K. C. Seok, L. K. Hoon, C. Hag-Ju, H. Horii, K. W. Don, L. S. In, and L. M. Young, “Depletion layer thickness and Schottky type carrier injection at the interface between Pt electrodes and (Ba, Sr)TiO3 thin films,” *J. Appl. Phys.*, vol. 85, no. 1, pp. 287–95, 1999.

[19] C. T. Black and J. J. Welser, “Electric-field penetration into metals: consequences for high-dielectric-constant capacitors,” *IEEE Trans. Electron Devices*, vol. 46, no. 4, pp. 776–780, 1999.

[20] G. Catalan, B. Noheda, J. McAneney, L. J. Sinnamon, and J. M. Gregg, “Strain gradients in epitaxial ferroelectrics,” *Phys. Rev. B*, vol. 72, no. 2, pp. 20 102–1, 2005.

[21] M. M. Saad, P. Baxter, R. M. Bowman, J. M. Gregg, F. D. Morrison, and J. F. Scott, “Intrinsic dielectric response in ferroelectric nano-capacitors,” *J. Phys.: Condens. Matter*, vol. 16, no. 41, pp. 451–6, 2004.

[22] L. W. Chang, M. McMillen, F. D. Morrison, J. F. Scott, and J. M. Gregg, “Size effects on thin film ferroelectrics: Experiments on isolated single crystal sheets,” *Appl. Phys. Lett.*, vol. 93, no. 13, pp. 132 904–1–3, 2008.

[23] S. Yamamichi, H. Yabuta, T. Sakuma, and Y. Miyasaka, “(Ba+Sr)/Ti ratio dependence of the dielectric properties for (Ba 0.5Sr0.5)TiO3 thin films prepared by ion beam sputtering,” *Appl. Phys. Lett.*, vol. 64, no. 13, pp. 1644–1646, 1994.

[24] S. K. Streiffer, C. Basceri, C. B. Parker, S. E. Lash, and A. I. Kingon, “Ferroelectricity in thin films: The dielectric response of fiber-textured (BaxSr1-x)Ti1+yO3+z thin films grown by chemical vapor deposition,” *J. Appl. Phys.*, vol. 86, no. 8, pp. 4565–4575, 1999.

[25] T. Nakamura, Y. Yamanaka, A. Morimoto, and T. Shimizu, “Effect of oxygen pressure on (BaxSr1-x)TiO3 thin films by pulsed laser ablation,” *Jpn. J. Appl. Phys.*, vol. 34, no. 9 B, pp. 5150–5153, 1995.

[26] e. Ken-ya Hashimoto, *RF Bulk Acoustic Wave Filters for Communications.* Artech House, 2009.

[27] Avago Technologies, www.avagotech.com.

[28] TriQuint Semiconductor, www.tqs.com.

[29] Skyworks Solutions, Inc., www.skyworksinc.com.

[30] Epcos, www.epcos.com.

[31] W. Pan, P. Soussan, B. Nauwelaers, and H. A. C. Tilmans, “Design and fabrication of a surface micromachined frequency tunable film bulk acoustic resonator with an extended electrostatic tuning range,” in *Proc. IEEE Ultrason. Symp.*, 2005, pp. 1840–1843.

[32] W. Pang, H. Zhang, H. Yu, C. Y. Lee, and E. S. Kim, “Electrical frequency tuning of film bulk acoustic resonator,” *J. Microelectromech. Syst.*, vol. 16, no. 6, pp. 1303–1313, 2007.

[33] J. J. Kim, H. Zhang, W. Pang, H. Yu, and E. S. Kim, “Low phase noise, FBAR-based voltage controlled oscillator without varactor,” in *Int. Conf. Solid-State Sensors, Actuators and Microsyst. Dig.*, 2005, pp. 1063–1066.

[34] M. Schreiter, R. Gabl, D. Pitzer, R. Primig, and W. Wersing, “Electro-acoustic hysteresis behaviour of PZT thin film bulk acoustic resonators,” *J. Eur. Ceram. Soc.*, vol. 24, no. 6, pp. 1589–1592, 2004.

[35] P. Muralt, J. Conde, A. Artieda, F. Martin, and M. Cantoni, “Piezoelectric materials parameters for piezoelectric thin films in GHz applications,” *Int. J. Microwave Wireless Technolog.*, vol. 1, no. 01, pp. 19–27, 2009.

[36] K. M. Lakin, K. T. McCarron, and J. F. McDonald, “Temperature compensated bulk acoustic thin film resonators,” in *Proc. IEEE Ultrason. Symp.*, 2000, pp. 855–8.

[37] R. Lanz, “Piezoelectric thin films for bulk acoustic wave resonator applications: From processing to microwave filters,” Ph.D. dissertation, École Polytechnique Fédérale de Lausanne, 2004.

[38] S. Ohta, K. Nakamura, A. Doi, and Y. Ishida, “Temperature characteristics of solidly mounted piezoelectric thin film resonators,” in *Proc. IEEE Ultrason. Symp.*, 2003, pp. 2011–2015.

[39] K. M. Lakin, J. Belsick, J. F. McDonald, and K. T. McCarron, “Improved bulk wave resonator coupling coefficient for wide bandwidth filters,” in *Proc. IEEE Ultrason. Symp.*, 2001, pp. 827–31.

[40] M. Norling, “Piezoelectric and ferroelectric device technologies for microwave oscillators,” Ph.D. dissertation, Chalmers University of Technology, 2009.

[41] K. M. Lakin, “Thin film resonator technology,” *IEEE Trans. Ultrason., Ferroelect., Freq. Contr.*, vol. 52, no. 5, pp. 707–716, 2005.

[42] S. Gevorgian and A. Vorobiev, “Impact of the electrodes on the tunability of paraelectric BST film based FBARs,” in *Proc. EuMC*, 2010, pp. 1210–1213.

[43] A. Vorobiev, J. Berge, and S. Gevorgian, “Thin film Ba0.25Sr0.75TiO3 varactors on Au bottom electrode for microwave applications,” in *Proc. EuMC*, 2006, pp. 839–842.

[44] K. Sreenivas, I. Reaney, T. Maeder, N. Setter, C. Jagadish, and R. G. Elliman, “Investigation of Pt/Ti bilayer metallization on silicon for ferroelectric thin film integration,” *J. Appl. Phys.*, vol. 75, no. 1, pp. 232–9, 1994.

[45] P. J. Moller, S. A. Komolov, and E. F. Lazneva, “Total current spectroscopy study of metal oxide surfaces: II. Unoccupied electronic states on TiO2(110) and SrTiO3(100) surfaces,” *J. Phys.: Condens. Matter*, vol. 12, no. 35, pp. 7705–7711, 2000.

[46] A. Vorobiev and S. Gevorgian, “Tunable thin film bulk acoustic wave resonators with improved Q-factor,” *Appl. Phys. Lett.*, vol. 96, no. 21, pp. 212 904–1–3, 2010.

[47] K. M. Lakin, G. R. Kline, and K. T. McCarron, “High-Q microwave acoustic resonators and filters,” *IEEE Trans. Microw. Theory Tech.*, vol. 41, no. 12, pp. 2139–46, 1993.

[48] A. Noeth, T. Yamada, V. O. Sherman, P. Muralt, A. K. Tagantsev, and N. Setter, “Tuning of direct current bias-induced resonances in micromachined Ba0.3Sr0.7TiO3 thin-film capacitors,” *J. Appl. Phys.*, vol. 102, no. 11, pp. 114 110–1–7, 2007.

[49] I. B. Vendik, P. A. Turalchuk, O. G. Vendik, and J. Berge, "Modeling tunable bulk acoustic resonators based on induced piezoelectric effect in BaTiO3 and Ba0.25Sr0.75TiO3 films," *J. Appl. Phys.*, vol. 103, no. 1, pp. 014 107–1–6, 2008.

[50] D. A. Berlincourt, D. R. Curran, H. Jaffe, "Piezoelectric and piezomagnetic materials and their function in transducers," in *Physical Acoustics*, W. P. Mason, Ed., London, U.K.: Academic Press 1964, vol. 1, pt. A.

[51] I. J. D. Larson, P. D. Bradley, S. Wartenberg, and R. C. Ruby, "Modified Butterworth-Van Dyke circuit for FBAR resonators and automated measurement system," in *Proc. IEEE Ultrason. Symp.*, 2000, pp. 863–8.

[52] M. Norling, J. Berge, and S. Gevorgian, "Parameter extraction for tunable TFBARs based on BaxSr1-xTiO3," in *IEEE MTT-S Int. Microw. Symp. Dig.*, 2009, p. 101.

[53] J. F. Rosenbaum, *Bulk acoustic wave theory and devices.* Artech House, Boston, 1988.

[54] S. Marksteiner, J. Kaitila, G. G. Fattinger, and R. Aigner, "Optimization of acoustic mirrors for solidly mounted BAW resonators," in *Proc. IEEE Ultrason. Symp.*, 2005, pp. 329–332.

[55] B. Razavi, *RF Microelectronics.* Prentice Hall, 1998.

[56] R. Thalhammer, G. Fattinger, M. Handtmann, and S. Marksteiner, "Ohmic effects in BAW-resonators," in *IEEE MTT-S Int. Microw. Symp. Dig.*, 2006, p. 4 pp.

[57] R. Thalhammer, J. Kaitila, R. Aigner, and S. Marksteiner, "Prediction of BAW resonator performance using experimental and numerical methods," in *Proc. IEEE Ultrason. Symp.*, 2004, pp. 282–5.

[58] A. Vorobiev, J. Berge, S. Gevorgian, M. Loffler, and E. Olsson, "Effect of interface roughness on acoustic loss in tunable thin film bulk acoustic wave resonators," *J. Appl. Phys.*, vol. 110, no. 2, pp. 024 116–4, 2011.

[59] A. Vorobiev, "Correlations between microstructure and Q-factor of tunable thin film bulk acoustic wave resonators," *J. Appl. Phys.*, vol. 110, no. 5, p. 054102, 2011.

[60] G. N. Saddik, D. S. Boesch, S. Stemmer, and R. A. York, "dc electric field tunable bulk acoustic wave solidly mounted resonator using SrTiO3," *Appl. Phys. Lett.*, vol. 91, no. 4, pp. 043 501–1, 2007.

[61] G. N. Saddik, D. S. Boesch, S. Stemmer, and R. A. York, “Strontium titanate DC electric field switchable and tunable bulk acoustic wave solidly mounted resonator,” in *IEEE MTT-S Int. Microw. Symp. Dig.*, 2008, pp. 1263–1266.

[62] A. Volatier, E. Defay, M. Aid, A. N’Hari, P. Ancey, and B. Dubus, “Switchable and tunable strontium titanate electrostrictive bulk acoustic wave resonator integrated with a Bragg mirror,” *Appl. Phys. Lett.*, vol. 92, no. 3, pp. 032 906–3, 2008.

[63] A. Noeth, T. Yamada, V. O. Sherman, P. Muralt, A. K. Tagantsev, and N. Setter, “DC bias-dependent shift of the resonance frequencies in BST thin film membranes,” *IEEE Trans. Ultrason., Ferroelect., Freq. Contr.*, vol. 54, no. 12, pp. 2487–2492, 2007.

[64] A. Noeth, T. Yamada, P. Muralt, A. K. Tagantsev, and N. Setter, “Tunable thin film bulk acoustic wave resonator based on paraelectric Ba0.3Sr0.7TiO3 thin film,” in *Proc. Electroceramics XI*, 2008.

[65] X. Zhu, J. D. Phillips, and A. Mortazawi, “A DC voltage dependant switchable thin film bulk wave acoustic resonator using ferroelectric thin film,” in *IEEE MTT-S Int. Microw. Symp. Dig.*, 2007, pp. 671–4.

[66] B. Ivira, A. Reinhardt, E. Defay, and M. Aid, “Integration of electrostrictive Ba0.7Sr0.3TiO3 thin films into bulk acoustic wave resonator for RF-frequency tuning under DC bias,” in *Proc. IEEE Int. Freq. Control Symp.*, 2008, pp. 254–258.

[67] X. Zhu, V. Lee, J. Phillips, and A. Mortazawi, “An intrinsically switchable FBAR filter based on barium titanate thin films,” *IEEE Microw. Wireless Compon. Lett.*, vol. 19, no. 6, pp. 359–361, 2009.

[68] G. N. Saddik and R. A. York, “An L-section DC electric field switchable bulk acoustic wave solidly mounted resonator filter based on Ba0.5Sr0.5TiO3,” in *Proc. IEEE Int. Symp. Appl. Ferroelect.*, 2011, pp. 1–4.

[69] G. N. Saddik and R. A. York, “Capacitively coupled dc voltage switchable barium strontium titanate solidly mounted resonator filter,” in *IEEE MTT-S Int. Microw. Symp. Dig.*, 2011, pp. 1–4.